

The importance of being discrete - An agent-based model for active nematics and more

Mathieu Dedenon,^{1,2,*} Carles Blanch-Mercader,^{3,†} Karsten Kruse,^{1,2,‡} and Jens Elgeti^{4,§}

¹Department of Biochemistry, University of Geneva, 1211 Geneva, Switzerland

²Department of Theoretical Physics, University of Geneva, 1211 Geneva, Switzerland

³Institut Curie, PSL Research University, CNRS UMR 168; F-75005 Paris, France

⁴Theoretical Physics of Living Matter, Institute of Biological Information Processing and Institute for Advanced Simulation, Forschungszentrum Jülich, Jülich, Germany

Living systems are composed of discrete units, assembled through a hierarchy of structures, and active, by locally extracting energy from their environment to produce mechanical work. Hydrodynamic theories have been successfully applied to describe the large scale dynamics of active materials. Yet, the hydrodynamic limit requires a separation of scales which is not necessarily fulfilled among living systems. In this work, we propose a novel agent-based model of flexible rods exchanging active force dipoles with nematic symmetry, allowing us to explore their behavior down to the sub-agent scale. We obtain spontaneous flows and self-propulsion of $+1/2$ topological defects, hallmarks of the hydrodynamic theory of active nematics, even on scales smaller than the individual agent! Moreover, our results go beyond the hydrodynamic framework, identifying novel correlations between orientation and flows or strong asymmetries between contractile and extensile activity. Finally, we show the versatility of our agent-based model by presenting spontaneous flows in three dimensions and nematic tissue growth. Because living systems like cell tissues often exhibit several sources of activity, our framework opens the way for more integrated descriptions of living materials.

I. INTRODUCTION

Living systems are maintained out of thermodynamic equilibrium as its constituents continuously convert chemical energy from its environment into other forms of energy. For example, suspensions of purified cytoskeletal proteins can exhibit turnover (assembly/disassembly), which can lead to self-propulsion (treadmilling) [1–6], and contractile or extensile mechanical stress generated by molecular motor activity [7–9]. Liquid crystalline order is present in numerous examples of living matter, such as the cytoskeleton, cultures of elongated cells, among many other examples [10–15]. There, microscopic constituents usually have polar or nematic anisotropy, and generate a nematic order at larger scales [16, 17]. Together with the activity of living matter, liquid crystalline order often leads to anisotropic active stress [18, 19], which plays a central role, for instance, in chromosome segregation [20], establishment of the anterior-posterior axis in *Caenorhabditis elegans* [21], or convergence-extension during wing development in *Drosophila melanogaster* [22]. The orientational order is often associated with topological defects, which play an important role in numerous biological processes such as stress organization, shape formation or density accumulation [23–26].

The physics of living matter has been studied theoretically using two main approaches. Hydrodynamic theories describe the dynamics of a small number of coarse-

grained physical variables [19]. The governing equations have a firm basis in symmetry arguments and conservation laws. In this approach, the link between the coarse-grained material parameters and the microscopic parameters is unknown and the length scales on which they become valid are unclear. Hallmarks of active nematic fluids such as spontaneous shear flows [27–30] or spontaneous defect unbinding [7, 31] were first discovered using this type of approach. Several numerical methods have been used to study the bulk properties of active nematics, such as spectral methods [32], Lattice-Boltzmann [33] or multi-particle collision dynamics [34–36]. Recent developments in numerical methods allow for studying active nematic fluids on dynamic surfaces [37–39].

Agent-based models provide a complementary approach. The dynamics of individual agents depends on a set of parameters that capture microscopic properties of the agents. Bridging the gap to smaller length scales, and allowing to test the validity of hydrodynamic models on small length scales. Those models have led to the discovery of long-range orientational order in two-dimensional active systems [40], or illustrate concepts like homeostatic pressure [41]. Most importantly however, an agent based model allows to easily avoid common assumptions of continuum theory like constant density or homogeneity of activity and retains the granular nature of active systems. This leads to important discoveries like motility-induced phase separation or negative homeostatic pressure. In this framework, activity is typically introduced in the form of agent self-propulsion [40, 42, 43] or agent turnover [41, 44].

Finally, living systems are complex and they often present numerous active processes. For instance, cells exert active force dipoles to their neighbors, while they also crawl and self-replicate. Therefore, it is important

* mathieu.dedenon@unige.ch

† carles.blanch-mercader@curie.fr

‡ karsten.kruse@unige.ch

§ j.elgeti@fz-juelich.de

to develop frameworks that allow to study possible interplays among these ingredients with a minimal set of variables and parameters.

In this work we develop a versatile agent-based model for active nematics to uncover the role of granularity. Basing our model on earlier models of tissue growth [41, 45, 46] gives us a model that can easily be extended to include other forms of activity, such as growth or division. In our model, each agent consists of a chain of particles, interacting with other agents via passive forces like excluded volume or short-ranged attraction, as well as active force dipoles. We use this model to study the spontaneous emergence of orientational order and flows in active nematic fluids, and how granularity results in further effects. Our simulations show, that phenomena uncovered by hydrodynamic analysis can be found down to sub-agent length scales. In channel geometries, we found novel correlations between the nematic orientational field and the flows of agents. The fluctuations naturally present in our simulations lead to dynamic flow fields with bursts of activity and spontaneous creation of topological defects. For large activity, we observe self-propulsion of $+1/2$ -defects with direction depending on the sign of the activity parameter, as well as density variations around the defect core. Furthermore our results evidences strong asymmetries in the collective behavior of agents with either extensile or contractile force dipoles. Finally, we show how this framework can be extended to three dimensions or include other active processes present in living systems like growth or self-propulsion.

II. AN AGENT-BASED MODEL OF AN ACTIVE NEMATIC LIQUID

In this section, we introduce an off-grid agent based model for an active nematic fluid. In our view, it is imperative that in the absence of an internal or external driving, our model imposes conservation of momentum and it relaxes to thermal equilibrium, i.e. it describes systems in a canonical ensemble with conserved hydrodynamic modes. To later introduce growth and division, we take inspiration from the two-particle growth model [41], which describes tissues of proliferating cells, and has already been extended to include polar activity [47, 48]. For non-conservative forces like activity and dissipation, we use a framework based on dissipative particle dynamics [49].

We consider N agents that each consist of N_p particles arranged in a stiff rod, Fig. 1a. Between two particles of the same agent, harmonic links with potential energy

$$V_l(\{\mathbf{r}\}) = \frac{K_l}{2} \sum_{p=0}^{N_p-2} (\ell_0 - r_{p,p+1})^2 \quad (1)$$

fix the distance between particles, where $r_{pq} = |\mathbf{r}_{pq}|$ with $\mathbf{r}_{pq} = \mathbf{r}_p - \mathbf{r}_q$ and \mathbf{r}_p is the position of particle p . Besides,

a bending energy

$$V_b(\{\mathbf{r}\}) = \frac{\kappa_b}{2\ell_0^3} \sum_{p=1}^{N_p-2} |\mathbf{r}_{p-1,p} - \mathbf{r}_{p,p+1}|^2 \quad (2)$$

ensures a rod-like shape. The parameter K_l is the spring constant for the harmonic potential, κ_b is the bending rigidity, and ℓ_0 is the equilibrium link length. The value of κ_b is chosen large enough to ensure an almost inextensible rod-like shape. Hence, the conservative part of the shape force on particle p is $\mathbf{F}_p^{(c,s)} = \mathbf{F}_p^{(l)} + \mathbf{F}_p^{(b)}$, where $\mathbf{F}_p^{(l)} = -\partial V_l / \partial \mathbf{r}_p$ and $\mathbf{F}_p^{(b)} = -\partial V_b / \partial \mathbf{r}_p$, see Fig. 1a.

Between two particles from different agents, a conservative interacting force $\mathbf{F}_{pq}^{(c,i)} = F^i(r_{pq})\hat{\mathbf{r}}_{pq}$ with $\hat{\mathbf{r}}_{pq} = \mathbf{r}_{pq}/r_{pq}$ accounts for the steric repulsion of two agents at short distances and their attraction at intermediate distances. Specifically, we use

$$F^i(r) = \begin{cases} f_0 ((r_c/r)^3 - 1) - f_1 & \text{if } r < r_c \\ 0 & \text{otherwise} \end{cases}, \quad (3)$$

where the constant f_0 characterizes the repulsion between two agents, f_1 quantifies their attraction, whereas r_c is the cut-off-distance beyond which two particles do not interact, see Fig. 1c.

In addition, all particles interact via pairwise dissipative $\mathbf{F}^{(d)}$ and random $\mathbf{F}^{(r)}$ forces, Fig. 1b. For two particles p and q , which can belong to the same or to different agents, they are given by

$$\mathbf{F}_{pq}^{(d)} = -\xi \omega(r_{pq})^2 [\hat{\mathbf{r}}_{pq} \cdot (\mathbf{v}_p - \mathbf{v}_q)] \hat{\mathbf{r}}_{pq}, \quad (4)$$

$$\mathbf{F}_{pq}^{(r)} = \sqrt{2\xi k_B T / \delta t} \omega(r_{pq}) \eta_{pq} \hat{\mathbf{r}}_{pq}. \quad (5)$$

Here, $\mathbf{v}_p = d\mathbf{r}_p/dt$ is the velocity of particle p , $\omega(r)$ is a weight function of distance with $\omega(r < r_c) = 1 - r/r_c$ or $\omega(r \geq r_c) = 0$, ξ has dimensions of a friction constant, $k_B T$ is the effective thermal energy, and δt is the simulation time step. The random numbers η_{pq} are Gaussian distributed with zero mean and unit variance. In addition, $\eta_{pq} = \eta_{qp}$ to ensure reciprocity of the interactions. The form of the random and dissipative interaction forces ensure that the (passive) system relaxes to thermal equilibrium [49]. Furthermore, we consider two independent sources of dissipation and noise for shape or inter-agent interactions, with respective dissipative coefficients $\xi = \xi_s$ and $\xi = \xi_i$. Finally, since all force components are central, that is, along the inter-particle axis, linear and angular momentum are conserved.

The system evolves in time according to Newton's equation of motion for each particle p

$$m \frac{d\mathbf{v}_p}{dt} = \mathbf{F}_p^{(\text{ext})} + \mathbf{F}_p^{(c,s)} + \sum_{\substack{q \neq p \\ \text{same agent}}} (\mathbf{F}_{pq}^{(d,s)} + \mathbf{F}_{pq}^{(r,s)}) + \sum_{\substack{q \neq p \\ \text{different agents}}} (\mathbf{F}_{pq}^{(c,i)} + \mathbf{F}_{pq}^{(d,i)} + \mathbf{F}_{pq}^{(r,i)} + \mathbf{F}_{pq}^{(a)}) \quad (6)$$

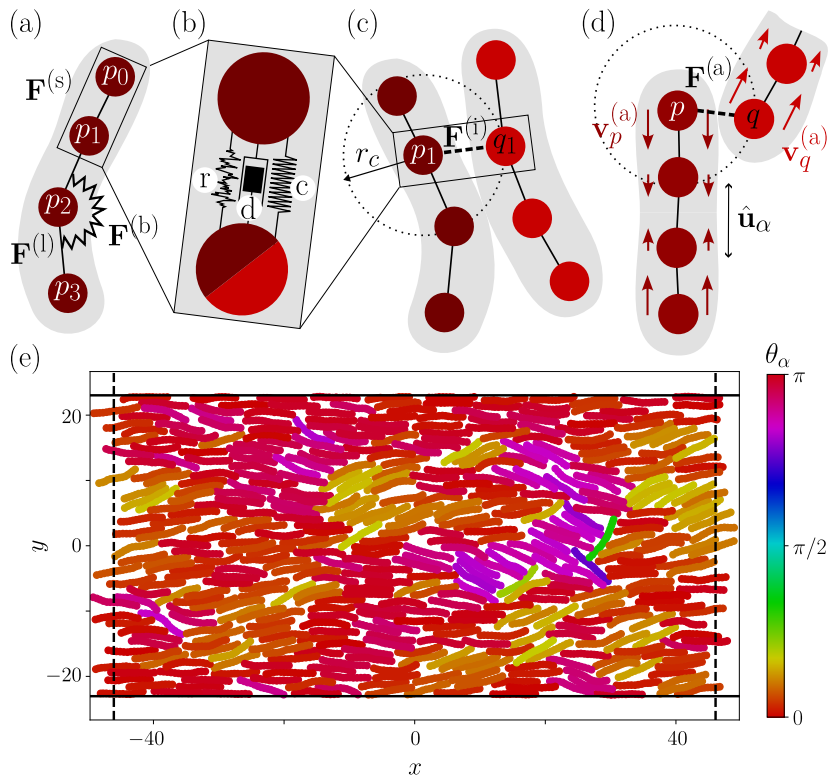


Figure 1. *A multi-particle agent-based model with internal active flows.* (a): Multi-particle agents (here $N_p = 4$ particles) have conservative shape interactions $\mathbf{F}^{(c,s)} = \mathbf{F}^{(l)} + \mathbf{F}^{(b)}$ between intra-agent particles, with link and bend components to ensure agent shape integrity. (b): The interaction between two particles comprises conservative (c), dissipative (d) and random components (r), for both intra-agent and inter-agent cases. (c): Inter-agent forces $\mathbf{F}^{(i)}$ between particles p_1, q_1 of different agents are short-ranged with cutting radius r_c (dotted circle). (d): An active force dipole is implemented as an internal treadmilling flow $\mathbf{v}_q^{(a)}$ (convergent here) over the particles of each agent, oriented along the agent axis with nematic symmetry. This flow renormalizes the velocities of particles $\mathbf{v}_p \mapsto \mathbf{v}_p + \mathbf{v}_p^{(a)}$ in the dissipative part of the inter-agent force $F^{(d,i)}$, giving an active force contribution $\mathbf{F}^{(a)}$. (e): Snapshot of an active system in the channel geometry, with periodic boundary conditions at $x = \pm L/2$ and confining wall at $y = \pm W/2$. Agents are color-coded according to their nematic orientation, indicated by the angle θ_α with respect to the horizontal axis. Parameters are $N = 30 \times 15$, $v_a = -3$.

The external force $\mathbf{F}_p^{(\text{ext})}$ could, for example, account for a confining wall. Besides, we can also consider a background friction force resulting from interactions with an underlying substrate in the form $\mathbf{F}_p^{(\text{d,ext})} = -\xi_e \mathbf{v}_p$. In this case, to maintain thermal properties in the passive case, we also need to add to Eq. (6) the random force $\mathbf{F}_p^{(\text{r,ext})} = \sqrt{2\xi_e k_B T / \delta t} \boldsymbol{\eta}_p$, where $\boldsymbol{\eta}_p$ is a vector with random components distributed as a Gaussian with zero mean and unit variance. The active force $\mathbf{F}_{pq}^{(a)}$ is the central part of our work and is detailed below. This system of equations is solved by temporal discretization, using a modified velocity-Verlet algorithm [50]. Further details of the numerical scheme used to integrate the dynamic equations can be found in Sect. S4.B-D [51].

So far, this system of equations describes a passive anisotropic material when $\mathbf{F}_{pq}^{(a)} = \mathbf{0}$. Next, we introduce an active force that is inspired by the retrograde flows of cytoskeletal filaments in cells, see Fig. 1d. Each particle p of an agent α generates a virtual active flow with

a prescribed velocity $\mathbf{v}_{a,p} = v_{a,p} \hat{\mathbf{u}}_\alpha$ oriented along the agent axis $\hat{\mathbf{u}}_\alpha$ (see SI Sect. 5 [51] for definition). The flow amplitude is

$$v_{a,p} = v_a \left(1 - \frac{2p}{N_p - 1} \right) \quad (7)$$

for $p = [0, N_p - 1]$, which varies linearly from peripheral to central particles and is controlled by the parameter v_a . Note that the velocity of the end particles is $v_a = v_{a,0} = -v_{a,N_p-1}$. Hence, for $v_a > 0$, the agent generates internal convergent flows, which we expect to result in a contractile active force dipole. Conversely, for $v_a < 0$, the force dipole is expected to be extensile.

The force of particle q on particle p generated in this active process is given by

$$\mathbf{F}_{pq}^{(a)} = -\xi_i \omega(r_{pq})^2 [\hat{\mathbf{r}}_{pq} \cdot (\mathbf{v}_{a,p} - \mathbf{v}_{a,q})] \hat{\mathbf{r}}_{pq}, \quad (8)$$

which has the same form as the dissipative interaction forces $\mathbf{F}^{(d)}$ in Eq. (4). The parameter ξ_i is the dissi-

pative coefficient from inter-agent interactions. We ignore active self-interactions between particles of the same agent. Consequently, a particle p with kinetic velocity \mathbf{v}_p will affect a neighbor q from another agent through an effective velocity $\mathbf{v}_p^* = \mathbf{v}_p + \mathbf{v}_{a,p}$, which combines kinetic and active effects.

To show the out-of-equilibrium nature of Eq. (8), we employ the formalism of the Rayleigh dissipation function \mathcal{R} [52]. The dissipative force on a particle p in Eq. (4), can be written as $\mathbf{F}_p^{(d)} = \sum_{q \neq p} \mathbf{F}_{pq}^{(d)} = -\partial \mathcal{R} / \partial \mathbf{v}_p$, where $\mathcal{R} = \frac{1}{2} \sum_{(p,q)} \xi \omega(r_{pq})^2 [\hat{\mathbf{r}}_{pq} \cdot (\mathbf{v}_p - \mathbf{v}_q)]^2$ and the sum is over all interacting pairs (p, q) . The scalar function \mathcal{R} is positive-definite and is even under time reversal and corresponds to energy dissipation. Similarly, the active force on a particle p can be derived from an active Rayleigh function \mathcal{R}_a , such that $\mathbf{F}_p^{(a)} = -\partial \mathcal{R}_a / \partial \mathbf{v}_p$ with

$$\mathcal{R}_a = \frac{1}{2} \sum_{(p,q)} \xi_i \omega(r_{pq})^2 [\hat{\mathbf{r}}_{pq} \cdot (\mathbf{v}_p - \mathbf{v}_q)] \cdot [\hat{\mathbf{r}}_{pq} \cdot (\mathbf{v}_{a,p} - \mathbf{v}_{a,q})] \quad (9)$$

Importantly, \mathcal{R}_a is not positive-definite and is odd under time reversal, so that it describes a power input. This procedure can be compared to the active Rayleigh function from the continuum theory of 2D incompressible active nematics [52], where one writes $\mathcal{R}_a = \int dS \mathbf{u} : \boldsymbol{\sigma}_a$ with the strain rate tensor $\mathbf{u} = (\nabla \mathbf{v} + (\nabla \mathbf{v})^T) / 2$ and the active stress $\boldsymbol{\sigma}_a$. Again, \mathcal{R}_a is odd under time-reversal and one obtains the active force density from $\nabla \cdot \boldsymbol{\sigma}_a = -\delta \mathcal{R}_a / \delta \mathbf{v}$.

The parameters of the model and their values are summarized in Table I in Sect. S4.A[51]. The units are chosen such that $m = r_c = 1$ and $\delta t = 10^{-3}$. To limit the influence of inertia on the system, parameter combinations are chosen such that inertial time scales are smaller than other relaxation time scales, see Sect. S4.A[51].

In this work, we choose a parameter set for which the system is in a nematic fluid phase at equilibrium, $v_a = 0$, Sect. S1[51]. Specifically, we choose a number of particles per agent $N_p = 14$ (i.e. particles of aspect ratio 7), a packing fraction $\text{pf} = 0.8$ (Sect. S4.F[51]), and a temperature $k_B T = 0.1$. The mean-squared displacement and the nematic orientation of the system varies with the packing fractions and with the temperatures as expected for other models of nematic liquid crystals [53, 54], see Fig. S1. Furthermore, unless otherwise stated, the initial condition corresponds to a set of evenly distributed agents that are aligned in the same direction, which is typically horizontal, Sect. S4.E[51].

In the following, we apply this new framework to classical situations of active nematics, and show that two hallmarks of active nematics, spontaneous flows and defect self-propulsion, are recovered.

III. SPONTANEOUS CHANNEL FLOW

To demonstrate the power of our model, we first study its behavior in the geometry of a 2d channel and show that spontaneous shear flows emerge for sufficiently large activity. For an active nematic fluid in a channel, the transition from a quiescent ordered state to a spontaneous flowing state was found using hydrodynamic theories [28, 33]. This phenomenon relies on an instability induced by the interplay between active stresses and the alignment of the nematic field to shear flows. For an assembly of rod-like agents, the instability occurs for extensible active stress at a finite threshold of activity [28, 33]. As we will show below, our agent-based model goes beyond hydrodynamic theories. For example, fluctuations lead to a non-monotonic dependence of the nematic order parameter on the activity of agents, as well as, correlations between shear flows and the nematic field for contractile activity.

Specifically, we simulate an assembly of active agents as introduced in Section II, confined in an infinite channel with periodicity L and width W , Fig. 1e. The longitudinal direction is represented by the coordinate x and the transverse direction by the coordinate y . We thus impose periodic boundaries in x and use harmonic confinement in y , with non-zero potential $V_{\text{conf}}(y) = K_w (|y| - W/2 + r_c/4)^2 / 2$ for $|y| > W/2 - r_c/4$, Sect. S4.C[51]. While the potential confines the agents in the y -direction, it does not affect their instantaneous velocity in the x -direction, equivalent to a perfect slip wall. Furthermore, the confining potential introduces an effective anchoring in y as agents tend to align parallel to the boundaries.

The system is characterized through a velocity and a nematic tensor fields $\mathbf{v}(\mathbf{r})$ and $\mathbf{Q}(\mathbf{r})$, which are computed by locally averaging the velocities and orientations of individual agents, respectively, see Sect. S5.B[51] for details. Furthermore, the nematic tensor field can be expressed as $\mathbf{Q} = s_n (2\hat{\mathbf{n}}\hat{\mathbf{n}} - \mathbf{1})$, where the variable $s_n(\mathbf{r})$ measures the local degree of nematic order: for a disordered phase $s_n = 0$ and for a perfectly nematic phase $s_n = 1$. Besides, the director field $\hat{\mathbf{n}}(\mathbf{r})$ represents the averaged orientation of a group of agents.

For sufficiently extensible activity, $v_a < 0$, a shear flow emerges, Fig. 2a. Indeed, in the two regions within the boundaries, the velocity field is mainly aligned along the x axis and it has opposite directions near $y = \pm W/2$. Individual agents exhibit persistent motion near the boundaries, whereas the trajectories of agents in the central region of the channel are more erratic Fig. 2b. Furthermore, the local nematic order parameter s_n is largely uniform throughout the channel and the director field $\hat{\mathbf{n}}$ aligns with the boundaries on average, see Fig. 2c. At any given time point, there is no consistent tilt of $\hat{\mathbf{n}}$ along the channel main axis.

To quantify the spatial organization of the velocity field, we projected the instantaneous velocity of individual agents onto a set of orthonormal modes: the product of a Fourier mode with wavenumber $k_x = 2\pi n_x / L$ in the

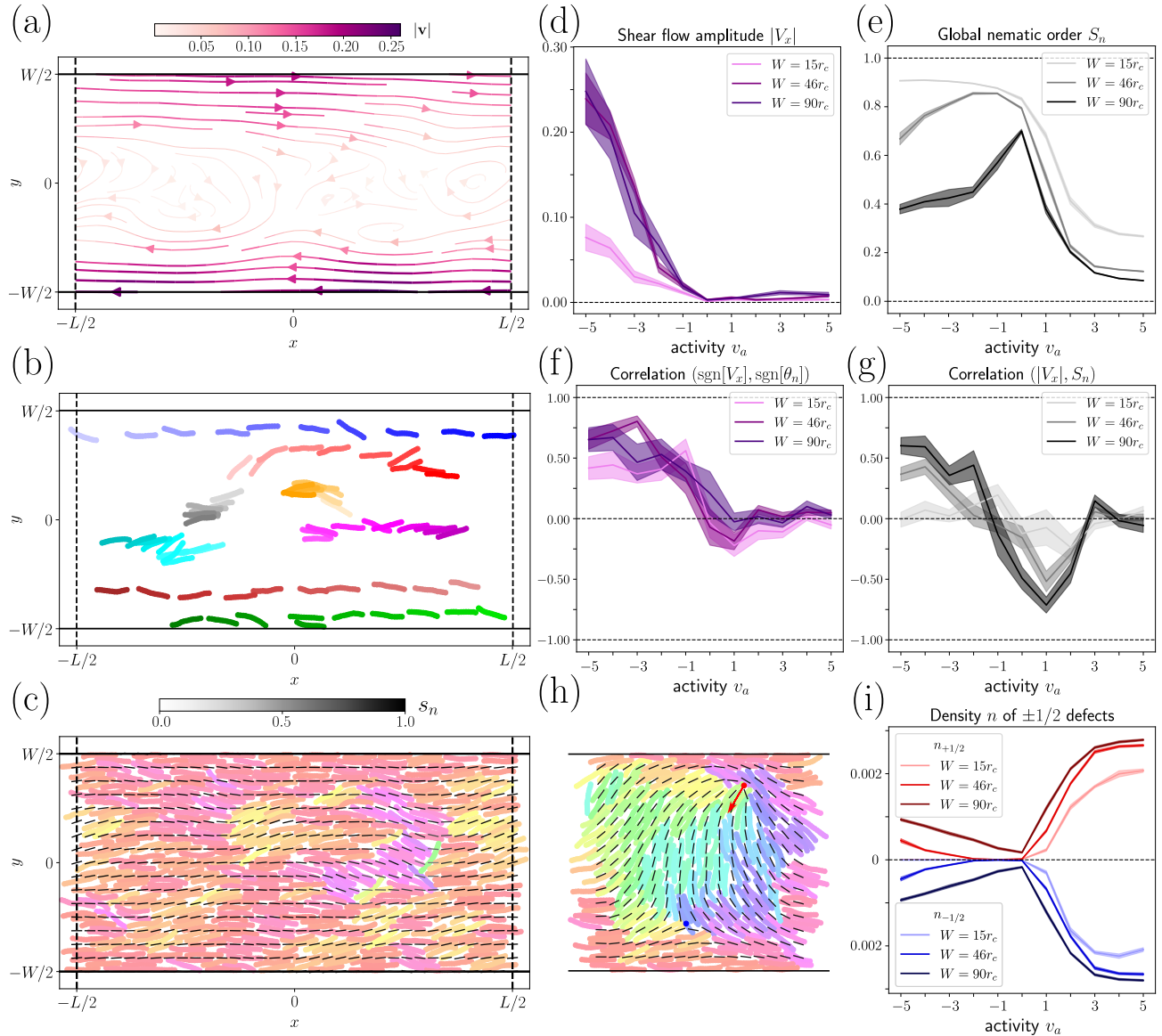


Figure 2. *Spontaneous channel flow.* (a): Coarse-grained velocity field $\mathbf{v}(\mathbf{r})$ for $v_a = -3$, $W = 46r_c$, at $t = 2500$. The colorscale indicates the velocity magnitude $|\mathbf{v}(\mathbf{r})|$. (b): Sequence of displacements of individual agents for a time interval $t = [4550 - 5000]$. The time sequence evolves from light to dark color. (c): Coarse-grained director field $\hat{\mathbf{n}}(\mathbf{r})$ in gray lines, for $v_a = -3$, $W = 46r_c$, at $t = 2500$, superposed with individual agent positions as in Fig. 1e. The gray colorscale indicates the local nematic order $s_n(\mathbf{r})$. (d): Shear flow amplitude $|V_x|$ as a function of v_a , for three values of W . (e): Global nematic order S_n as a function of v_a and different W , averaged over times and independent realizations. (f): Correlation of shear velocity V_x with director angle θ_n , as a function of v_a and W . (g): Correlation of shear flow amplitude $|V_x|$ with global nematic order S_n (gray), as a function of v_a and W . (h): Superposed nematic texture and particle positions indicating the presence of $+1/2$ and $-1/2$ defects, for $v_a = -5$ at $t = 1500$. (i): Density of $\pm 1/2$ defects averaged over time, as a function of v_a , for three values of W .

Parameters are $N = N_x \times N_y$ with $N_x = 30$ and $N_y = [5, 15, 30]$ corresponding to $W = [15, 46, 90]r_c$ and $L = 92r_c$, $t_{\text{sim}} = 5000$, $N_{\text{sim}} = [10, 20, 10]$. Curves indicate mean quantities averaged over independent runs, shaded regions indicate one standard deviation around the mean.

x direction and a Legendre polynomial with index n_y in the y direction, see Sect. S5.E[51] for details. Therefore, each mode is characterized by two integer numbers n_x and n_y . The mode associated with a pure shear of the x component of the velocity field is $(n_x, n_y) = (0, 1)$, and we name its amplitude the shear flow amplitude $|V_x|$.

Representing $|V_x|$ for varying values of v_a reveals a transition to spontaneous shear flows when $v_a < 0$, Fig. 2d. For extensile activity $v_a < 0$, as the agent's activity v_a decreases or as the channel width increases, the magnitude of the shear flow increases. Notably, shear flows were observed even for channel width as small as tens of particle

diameters ($W = 15r_c$), Fig. 2d and Fig. S2, where the hydrodynamic limit is expected to break down. For sufficiently large channel width, the magnitude of the shear mode saturates and the flow organization becomes more complex than a simple shear flow, Fig. S3. Finally, for contractile activity $v_a > 0$, the magnitude of the shear flow is nearly vanishing irrespective of the channel width.

Up to now, our findings are in qualitative agreement with past results from hydrodynamic theories. However, several observations in our simulations challenge this paradigm.

(i) In hydrodynamic theories, the instability occurs at a critical value of the active stress coefficient α_c that depends on the channel width W as $\alpha_c \propto -1/W^2$ when the director field is strongly anchored to the boundaries [28, 29]. In our agent-based simulations, the transition is observed in a range of the parameter v_a between -1 and 0 that does not depend on W , see Fig. 2d. Furthermore, for fixed channel width W and activity v_a , our simulations show that a critical value of the particles per agent $N_p \geq N_p^* \approx 10$ is necessary to trigger spontaneous shear flows, Fig. S4.

(ii) The hydrodynamic theories show that the shear flow state features a well-defined tilt of the director field [28, 29], which, together with the active stresses, influences the strength and the direction of shear flows. Specifically, for an extensile (contractile) fluid, a counterclockwise tilt of the director angle $\theta_n > 0$ induces flows with $v_x > 0$ ($v_x < 0$) in the upper boundary, and vice-versa. However, in our simulations, the director field largely aligns with the channel boundaries and tilts in both clockwise and counterclockwise directions, Fig. 2c. We then define the global director $\hat{\mathbf{n}}(t) = (\cos \theta_n(t), \sin \theta_n(t))$ by averaging the agents orientation over the whole channel, see Sect. S5.A[51]. The equal-time correlation between the sign of the director angle $\text{sgn}(\theta_n)$ and the sign of the shear flow amplitude $\text{sgn}(V_x)$ shows a correlation for $v_a < 0$, and a weaker anti-correlation for both $v_a > 0$ and narrow channels, Fig. 2f. Finally, a correlation between the magnitude of the shear flows and the global nematic order parameter S_n is found for $v_a < 0$ and increases in magnitude as the channel width increases, see Fig. 2g. For $v_a > 0$, an anti-correlation appears, see Fig. 2g.

(iii) For both contractile activity $v_a > 0$, as well as extensile activity $v_a < 0$ and sufficiently large channel width, the nematic field presents half-integer topological defect pairs that continuously nucleate and annihilate, see Fig. 2h-i and Sect. S5.C[51] for detection method. Concurrently, the global nematic order parameter S_n , defined in Sect. S5.A[51], depends on parameters as shown in Fig. 2e. Contractile activity ($v_a > 0$) reduces S_n , whereas extensile activity increases S_n for sufficiently narrow channels, Fig. 2e case $W = 15r_c$. Interestingly, one observes a decrease of S_n at larger amplitudes of $v_a < 0$ for sufficiently wide channels, Fig. 2e cases $W = 46r_c$ and $W = 90r_c$. This is consistent with the increased density of half-integer topological defect

pairs, Fig. 2i. For a fixed value of v_a , the density of defects increases by increasing the channel width W , which leads to a decrease in S_n . The combination of Fig. 2e,g,i shows that the flow profile alternates between coherent phases with high nematic order, and incoherent phases with nematic topological defects.

The results in this section confirm our expectation that the active forces due to internal flows can generate nematic activity: for $v_a > 0$ ($v_a < 0$) contractile (extensile) active stress is produced.

IV. BULK PROPERTIES - BEND-INSTABILITY INDUCED SPONTANEOUS FLOW REORIENTATION

In this section, we study the emergence of spontaneous flows in the bulk, and therefore without constraining walls. To model bulk properties, we use periodic boundary conditions in both directions with a fixed period set as $L = 30r_c$. Here, we first focus on a small system size, for which the system exhibits coherent collective motion. In the next section, we will discuss a larger system size, for which the collective dynamics is more irregular and topological defect abound.

Hydrodynamic theories of active nematic fluids show that for sufficiently large activity the bulk fluid exhibits dynamic flows and director patterns. However there are differences in the behavior near the instability threshold of an ordered state. Some works that in addition included a concentration field linked to the strength of the active stresses showed that above threshold, the fluid reaches a state where the director field alternates continuously between horizontal and vertical alignments with intermediate burst of activity and flows [55]. Some other works reported, dynamic and irregular velocity and director fields for low activity regimes [56]. Finally, other works that considered a defect-free active nematic fluid found above threshold that the system reaches a steady-state with a spatially-varying director and velocity fields [32].

For the same parameters as in Fig. 2a, an initial irregular velocity pattern self-organizes over time into an array of streams along the horizontal axis, Fig. 3b. The velocity within each stream alternates between the two horizontal directions, leading to shear flows between adjacent streams. In a second phase, the flow pattern evolves from a horizontal to a vertical arrangement of streams and the velocity within each stream alternates between the two vertical directions. Concurrently, the director field changes forms a horizontal alignment in the first phase, and then changes to a vertical alignment in the second phase, see Fig. 3a. During the transition periods, the director field bends and some topological defect pairs are created, see Fig. 3a third panel. At later times, the system keeps on repeating this sequence of events, and continuously switches between horizontal and vertical alignments, see [Movie XX](#).

The previous results suggest a temporal correlation between the director field and the velocity field. To quantify the direction of streams, we define a phenomenological nematic tensor $\mathbf{Q}_v = \langle 2\mathbf{v}_\alpha \mathbf{v}_\alpha - |\mathbf{v}_\alpha|^2 \mathbf{1} \rangle_\alpha / \langle |\mathbf{v}_\alpha|^2 \rangle_\alpha$ from the agent velocities \mathbf{v}_α . The average is performed over all agents in the periodic domain. Analogously to the nematic tensor field, \mathbf{Q}_v can be expressed as $\mathbf{Q}_v = S_v(2\hat{\mathbf{n}}_v \hat{\mathbf{n}}_v - \mathbf{1})$, where the variable S_v measures the degree of global nematic alignment of the set of agent's velocities. Besides, the field $\hat{\mathbf{n}}_v = (\cos(\theta_v), \sin(\theta_v))$ represents the averaged nematic orientation of agent's velocities, where θ_v is the phase with respect to the horizontal axis. Recall that we introduced above similar variables for the nematic tensor field of agent's orientation, where S_n and θ_n are the global nematic order parameter and the global nematic phase, respectively.

The values of S_n and S_v fluctuate in time and are correlated with a correlation factor that decreases for increasing activity, see Fig. 3c,e. The phases θ_n and θ_v also fluctuate in time and their distributions peak at both 0 or $\pi/2$ radians, corresponding to a horizontal and a vertical nematic alignment respectively, see Fig. 3d. The phases θ_n and θ_v are also correlated for the range of activity that was explored, see Fig. 3e. Indeed, the switching events between horizontal and vertical alignments occur almost concurrently for the director and velocity fields, see Fig. 3d. Besides, the distribution of the switching times between two consecutive events is well approximated by a single exponential, see Fig. S5a-d. The fitted characteristic time T_{res} decreases as the magnitude of agent activity increases, see Fig. 3f. This suggests that the switching events are asynchronous and there is no well-defined temporal period. Finally, the switching times match to the time points when S_n and S_v are nearly vanishing, see Fig. 3c,d.

V. DEFECT DYNAMICS

The results of the previous section point towards an important role of topological defects for the organization of the flow field in our agent-based system. Doubling the period at $L = 60r_c$, topological defects appear for $v_a < 0$ as well as for $v_a > 0$, Fig. 4a-c. Contrarily to a passive nematic material, there is a continuous creation of $\pm 1/2$ defect pairs driven by activity, balanced by annihilation events. However, the number of defects scales differently with v_a depending on the sign of v_a . Whereas their number continues to increase linearly with $|v_a|$ for $v_a < 0$, their number starts to saturate for $v_a \gtrsim 3$, Fig. 4b. This is in contrast to the hydrodynamic theory, where the number of defects depends on the absolute value of the activity $|\alpha|$ [57].

One can associate an orientation $\hat{\mathbf{p}} = \nabla \cdot \mathbf{Q} / |\nabla \cdot \mathbf{Q}|$ with $+1/2$ defects that points from their head to their tail, Fig. 4b. Due to the broken head-tail symmetry of the comet shape, $+1/2$ defects in active fluids can self-propel [7]. In our simulations, the fluid velocity $\mathbf{v}_{+1/2}$

at the position of $+1/2$ defects points on average in the direction of $-\hat{\mathbf{p}}$ if $v_a < 0$, Fig. 4a,d,e. In the opposite case, $\mathbf{v}_{+1/2}$ points into the direction of $\hat{\mathbf{p}}$, but its correlation with the defect direction is smaller, Fig. 4c,e,f. In parallel, we find that the component of $\mathbf{v}_{+1/2}$ orthogonal to $\hat{\mathbf{p}}$ vanishes on average for all values of v_a , Fig. S5e. We conclude that the direction of the fluid velocity $\mathbf{v}_{+1/2}$ at the position of $+1/2$ defects is different for $v_a > 0$ and $v_a < 0$, Fig. 4d. With the hydrodynamic framework, $+1/2$ defects move along the orientation of $\hat{\mathbf{p}}$, into the direction of their head in the case of an extensile fluid and in the opposite direction in the case of a contractile fluid [58–60]. This is again in agreement with our notion that $v_a < 0$ ($v_a > 0$) corresponds to an extensile (contractile) fluid.

One advantage of our particle-based framework is the intrinsic compressibility of the system, which allows to extract a coarse-grained density field. In Figure 4g,i we show the relative variation $\Delta\hat{\rho} = [\rho(\mathbf{r}) - \bar{\rho}]/\bar{\rho}$ of the local density $\rho(\mathbf{r})$ with respect to the global density $\bar{\rho} = N/(L_x L_y)$. We compute the dipole $D_{\rho,+1/2}$ of density variations at $+1/2$ defect sites, as defined in Fig. S5f-h. We find that, on average, for $v_a < 0$ there is a region of compression at the head and a region of dilation at the tail of a $+1/2$ defect and *vice versa* for $v_a \gtrsim 0$. This is in agreement with results from calculations within the hydrodynamic framework [61].

As for the spontaneous flow instability, the behavior of topological defects in our simulation framework exhibits on average features that are similar to that obtained from the hydrodynamic theory despite a small number of agents.

VI. SCOPE

While so far we have explored the active nematic fluid in two dimensional geometries, the key strength of our model lies in its versatility to include other boundary geometries and other forms of activity. The field of active matter is typically divided in subfields like dry or wet, polar or nematic active forces, mass conserving or growing matter [16, 44]. This division of fields is also reflected in the division of theoretical descriptions [62]. But while the fields are divided, the systems are not. Bacteria swim and divide, actin filaments are active nematics, while they also grow by assembly. Cells in eukaryotic tissues can crawl, generate nematic active stresses, and divide. These examples highlight the necessity of a broad and versatile model that would incorporate all forms of activity. Our model does exactly that.

While up to this point, we have explored assemblies in two dimensions, the particle-based nature of our model means that an extension to three dimensions does not require any change, except dimensionality and boundary conditions. To demonstrate this, we simulate a setup very similar to the channel geometry as in section III. Agents are confined to a channel along dimensions y, z ,

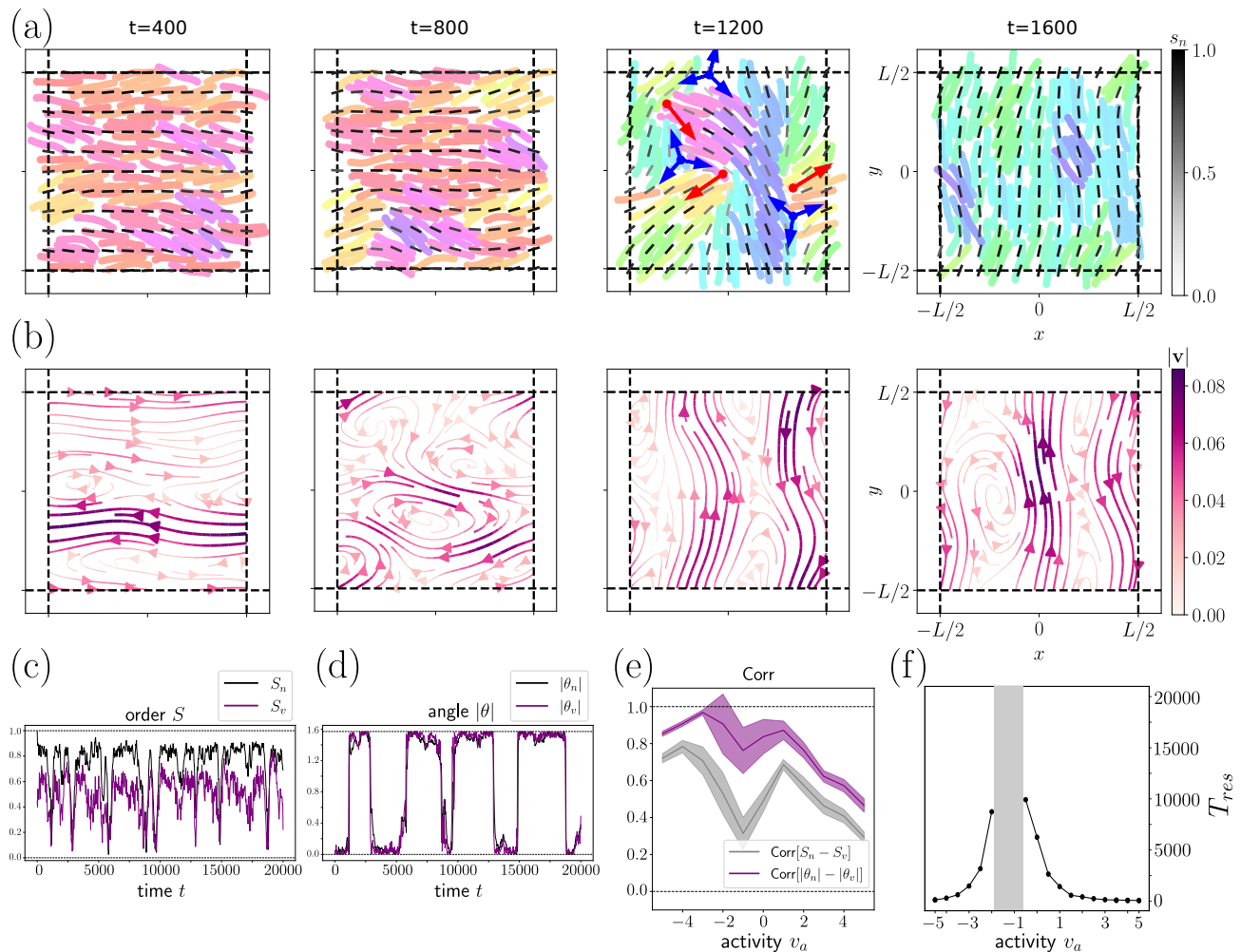


Figure 3. *Spontaneous flow in PBCs.* (a): Snapshots of the coarse-grained nematic field or agents positions for $v_a = -3$, at respective times $t = 400, 800, 1200, 1600$. (b): Snapshots of the coarse-grained velocity field for $v_a = -3$, corresponding to the times in (a). (c,d): Temporal evolution of nematic order S_n (c) and director orientation $|\theta|$ (d) for agent shape in black and agent velocity in purple. Same data as in (a,b). (e): Instantaneous correlation between S_n and S_v (gray) or between $|\theta_n|$ and $|\theta_v|$ as a function of activity v_a . (f): Exponential time T_{res} as a function of activity v_a , obtained from a fit of the distributions of switching times from horizontal to vertical velocity alignment. Parameters are $N = 10 \times 10$, $L = 30r_c$, $t_{sim} = 20000$, $N_{sim} = 20$.

with periodic boundary conditions along x . Fig. 5a shows a snapshot of the system and the resulting flow and orientation maps. We observe a shear flow pattern similar to Fig. 2a, but the flows are less localised to the walls. The escape of agents towards the third dimension appears to limit the nematic order and the coherency of the active flows.

Furthermore, our model is based on the two-particle growth model [41], which allows us to implement similarly growth, splitting and deletion mechanisms with mechanical feedback (see S4.G [51]). To further show the versatility in boundary conditions, Fig. 5b displays a group of agents growing on a circular patch with absorbing boundary. Agents escaping the patch are removed from the simulation. We see nematic order with typically two $+1/2$ defects close to the center, Fig. 5b. We observe

transient, spiral-like flows, reminiscent of those predicted for polar active gels [27, 63]. Divisions are primarily located at the periphery, as observed for tumor spheroids and in the two-particle growth model [46, 64–66].

These results demonstrate that our model can readily be extended to further forms of activity. In future works, we will also include polar activity - both dry and wet, in order to arrive at one model for all forms of activity within one framework.

VII. DISCUSSION

In this work, we present a new theoretical framework to describe active nematic fluids with a particle-based approach. We showed for finite system sizes that in-

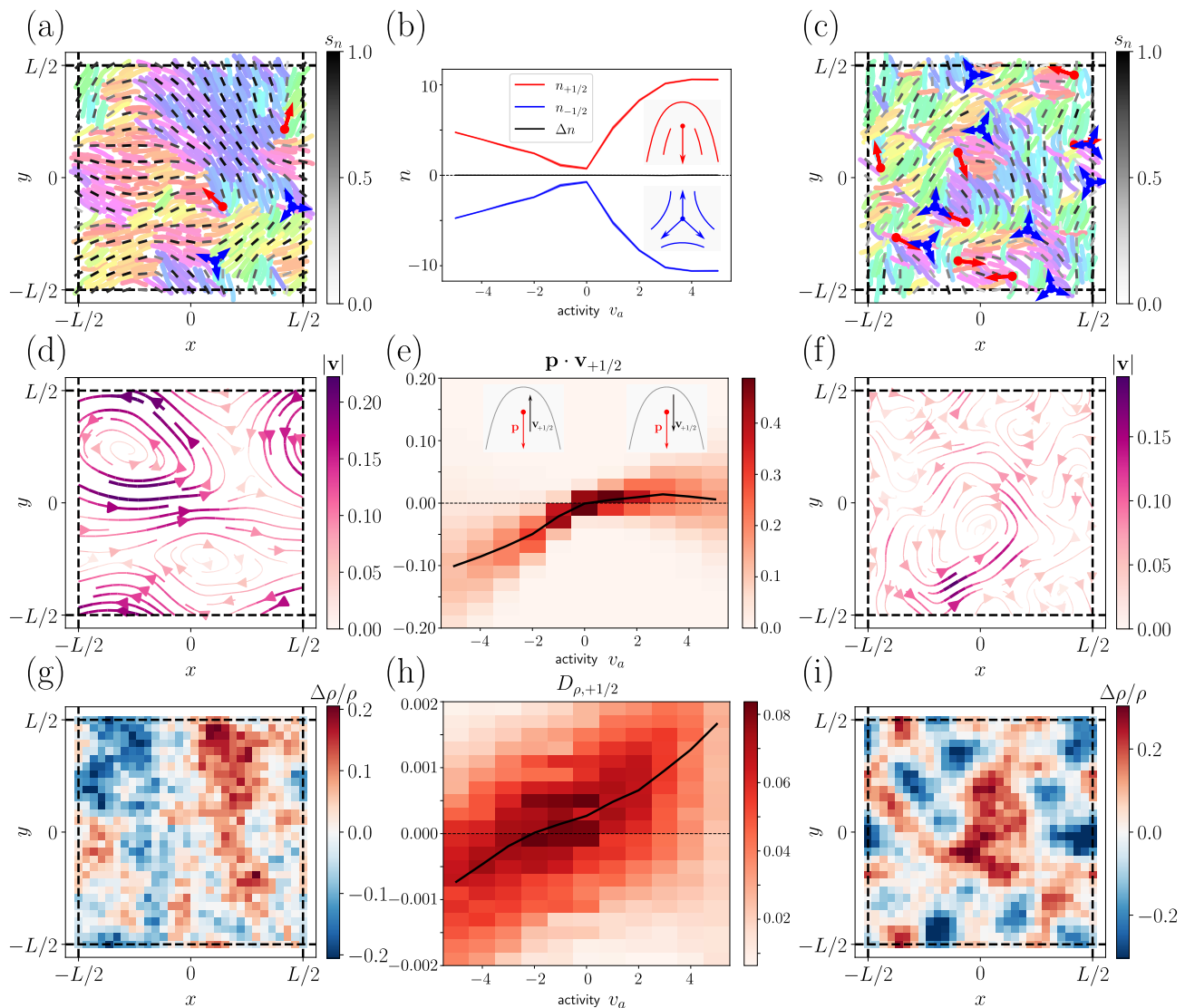


Figure 4. *Defect nucleation and self-propulsion.* **(a,d,g)**: Snapshots of the periodic system for $v_a = -4$, showing the agent orientations and nematic texture **(a)**, the velocity field **(d)** and the relative density variations **(g)**. **(b)**: Variation of the $+1/2$ (red) and $-1/2$ (blue) defect densities as a function of activity, with net defect charge density $\Delta n = n_{+1/2} - n_{-1/2}$ (black). **(c,f,i)**: Snapshots of the periodic system for $v_a = 4$, showing the agent orientations and nematic texture **(c)**, the velocity field **(f)** and the relative density variations **(i)**. **(e)**: Density histogram as a function of activity of the $+1/2$ -defect core velocity $\mathbf{v}_{+1/2}$ projected along the defect polarity $\hat{\mathbf{p}}$. **(h)**: Density histogram as a function of activity of the density dipole $D_{\rho,+1/2}$, representing the local variation of density along the axis defined by the polarity $\hat{\mathbf{p}}$ (inset), over a surface patch A . Here A is 7×7 pixels centered on the defect core position $\mathbf{r}_{+1/2}$, with one pixel $\approx 2.1r_c$. Parameters are $N = 20 \times 20$, $L = 60r_c$, $N_{\text{sim}} = 20$.

corporation of internal active flows with nematic symmetry give rise to spontaneous flows and self-propulsion of $+1/2$ -defects, which are well-known hallmarks of active nematic fluids. This establishes a qualitative correspondence between the mesoscopic scale where individual agents generate active force dipoles, and the hydrodynamic scale with the active nematic stress $\boldsymbol{\sigma}^{(a)} = \alpha \mathbf{Q}$.

There are several motivations for the introduction of this new framework. The difficulty to design well-controlled experimental systems of active matter makes *in silico* experiments provided by agent-based simula-

tions useful to decipher between hypothetical mechanisms. For instance, the ability to control the forces exchanged by individual units facilitates intuition and will help to clarify the emergence of active stress. Second, experimental realisations of active systems like cell tissues or cell cytoskeleton often involve few hundreds or thousands of agents. The continuous limit of hydrodynamics is an approximation, where higher order terms are usually neglected for simplicity, and it is important to check at a mesoscopic scale if the expected results from the hydrodynamic theory are preserved for small

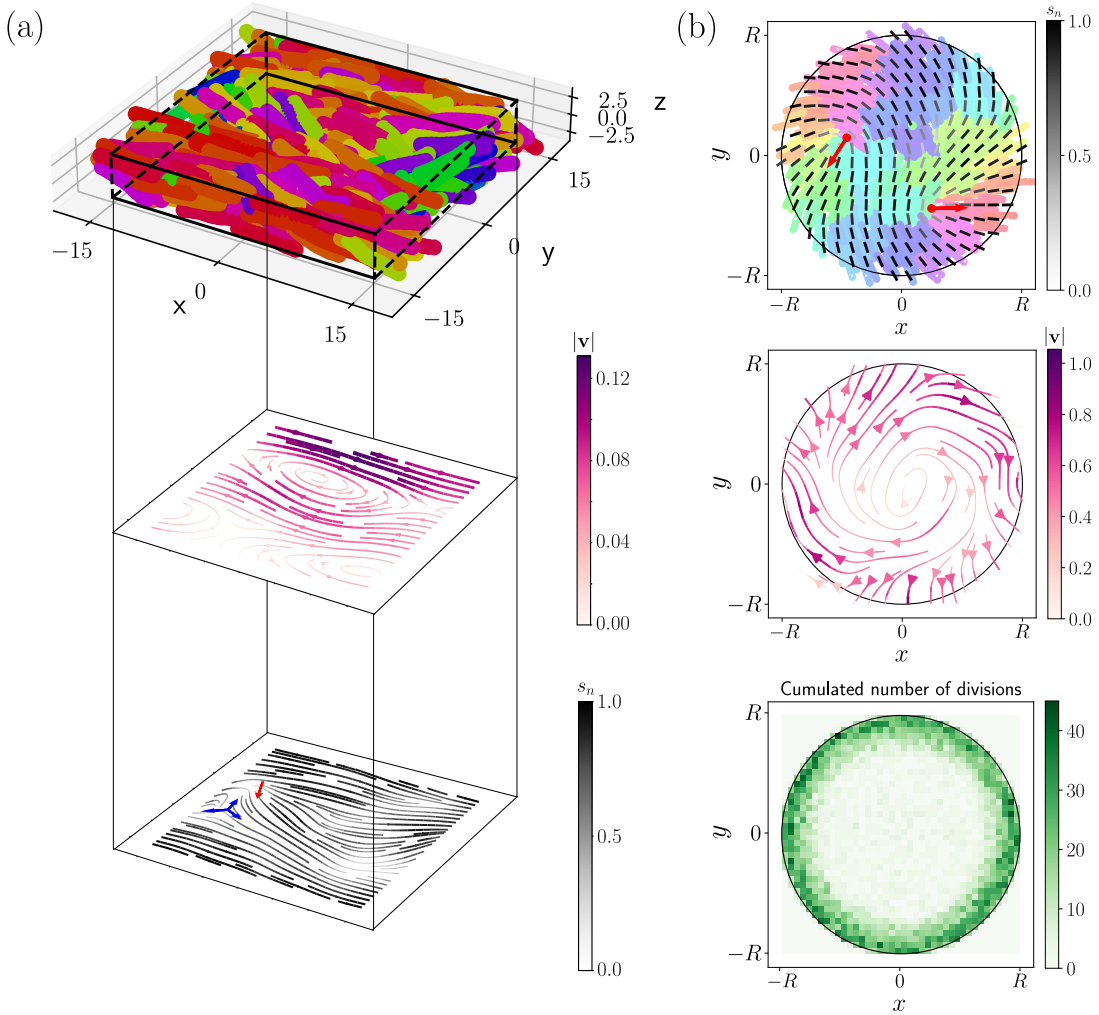


Figure 5. *3D flow and 2D tissue growth.* (a): 3D system with confinement along y, z directions and periodic boundary conditions along x , with $N = 10 \times 10 \times 4$, $v_a = -1$, $k_B T = 0.05$ and $\xi_s = 20$, $\xi_i = 40$. Top panel indicates a snapshot of particles positions, middle panel the coarse-grained velocity field projected in the xy -plane at $z = 0$, and bottom panel the coarse-grained nematic field, at $t = 1500$. (b): 2D system with cell divisions and absorbing boundary (circle of radius $R = 18r_c$), initiated with $N = 1$ agent, $N_p = 8$ particles per agent, $v_a = 0$, $\xi_s = 20$, $\xi_i = 40$ and $\kappa_b = 120$. Top panel indicates a snapshot of particles positions superposed with the nematic texture, middle panel the coarse-grained velocity field, and bottom panel the spatial distribution of the cumulated number of divisions.

number of agents. Third, fluctuations can play an important role, especially near a phase transition, or when number of constituents is small. Our agent based model also naturally accounts for fluctuations. And indeed, we see that these fluctuations for example cause a re-orientation of global flow patterns. In particular, agent turnover is intrinsically a micro-scale process, and it is important to account for the discreteness of the active entities [44]. Third, another advantage of agent-based models over continuous descriptions is the emergent rheological response, for instance activity might trigger local compression in the system and reduce fluidity through

effective viscosity. These density-dependent effects are difficult to capture at the hydrodynamic level except by postulating specific dependencies on chosen parameters. Last, but importantly, our agent-based model is versatile and can easily be extended to more complex geometries, composite systems, and multiple sources of activity, in particular agent turnover or agent self-propulsion.

ACKNOWLEDGMENTS

The computations were performed at University of Geneva on Baobab HPC cluster.

- [1] E. D. Korn, Actin polymerization and its regulation by proteins from nonmuscle cells., *Physiological reviews* **62**, 672 (1982).
- [2] L. Blanchoin, R. Boujemaa-Paterski, C. Sykes, and J. Plastino, Actin dynamics, architecture, and mechanics in cell motility, *Physiological reviews* **94**, 235 (2014).
- [3] G. J. Brouhard and L. M. Rice, Microtubule dynamics: an interplay of biochemistry and mechanics, *Nature reviews Molecular cell biology* **19**, 451 (2018).
- [4] H. V. Goodson and E. M. Jonasson, Microtubules and microtubule-associated proteins, *Cold Spring Harbor perspectives in biology* **10**, a022608 (2018).
- [5] M. Dogterom and G. H. Koenderink, Actin–microtubule crosstalk in cell biology, *Nature reviews Molecular cell biology* **20**, 38 (2019).
- [6] B. L. Goode, J. Eskin, and S. Shekhar, Mechanisms of actin disassembly and turnover, *Journal of Cell Biology* **222**, e202309021 (2023).
- [7] T. Sanchez, D. T. N. Chen, S. J. DeCamp, M. Heymann, and Z. Dogic, Spontaneous motion in hierarchically assembled active matter, *Nature* **491**, 431–434 (2012).
- [8] Y. Ideses, V. Erukhimovitch, R. Brand, D. Jourdain, J. S. Hernandez, U. R. Gabinet, S. A. Safran, K. Kruse, and A. Bernheim-Groswasser, Spontaneous buckling of contractile poroelastic actomyosin sheets, *Nature Communications* **9**, 10.1038/s41467-018-04829-x (2018).
- [9] L. Haviv, D. Gillo, F. Backouche, and A. Bernheim-Groswasser, A cytoskeletal demolition worker: myosin ii acts as an actin depolymerization agent, *Journal of molecular biology* **375**, 325 (2008).
- [10] R. Kemkemer, D. Kling, D. Kaufmann, and H. Gruler, Elastic properties of nematoid arrangements formed by amoeboid cells, *The European Physical Journal E* **1**, 215 (2000).
- [11] G. Duclos, S. Garcia, H. G. Yevick, and P. Silberzan, Perfect nematic order in confined monolayers of spindle-shaped cells, *Soft Matter* **10**, 2346–2353 (2014).
- [12] H. Morales-Navarrete, H. Nonaka, A. Scholich, F. Segovia-Miranda, W. de Back, K. Meyer, R. L. Bogorad, V. Kotliansky, L. Bruschi, Y. Kalaidzidis, *et al.*, Liquid-crystal organization of liver tissue, *Elife* **8**, e44860 (2019).
- [13] A. Comba, S. M. Faisal, P. J. Dunn, A. E. Argento, T. C. Hollon, W. N. Al-Holou, M. L. Varela, D. B. Zamlar, G. L. Quass, P. F. Apostolides, *et al.*, Spatiotemporal analysis of glioma heterogeneity reveals *colla1* as an actionable target to disrupt tumor progression, *Nature communications* **13**, 3606 (2022).
- [14] J. Eckert, B. Ladoux, R.-M. Mège, L. Giomi, and T. Schmidt, Hexanematic crossover in epithelial monolayers depends on cell adhesion and cell density, *Nature Communications* **14**, 5762 (2023).
- [15] T. B. Saw, W. Xi, B. Ladoux, and C. T. Lim, Biological tissues as active nematic liquid crystals, *Advanced materials* **30**, 1802579 (2018).
- [16] M. C. Marchetti, J. F. Joanny, S. Ramaswamy, T. B. Liverpool, J. Prost, M. Rao, and R. A. Simha, Hydrodynamics of soft active matter, *Reviews of Modern Physics* **85**, 1143–1189 (2013).
- [17] A. Doostmohammadi, J. Ignés-Mullol, J. M. Yeomans, and F. Sagués, Active nematics, *Nature Communications* **9**, 10.1038/s41467-018-05666-8 (2018).
- [18] K. Kruse and F. Jülicher, Actively contracting bundles of polar filaments, *Physical Review Letters* **85**, 1778–1781 (2000).
- [19] J. Prost, F. Jülicher, and J.-F. Joanny, Active gel physics, *Nature Physics* **11**, 111–117 (2015).
- [20] J. Brugués and D. Needleman, Physical basis of spindle self-organization, *Proceedings of the National Academy of Sciences* **111**, 18496–18500 (2014).
- [21] M. Mayer, M. Depken, J. S. Bois, F. Jülicher, and S. W. Grill, Anisotropies in cortical tension reveal the physical basis of polarizing cortical flows, *Nature* **467**, 617–621 (2010).
- [22] R. Etournay, M. Popović, M. Merkel, A. Nandi, C. Blasse, B. Aigouy, H. Brandl, G. Myers, G. Salbreux, F. Jülicher, and S. Eaton, Interplay of cell dynamics and epithelial tension during morphogenesis of the drosophila pupal wing, *eLife* **4**, 10.7554/elife.07090 (2015).
- [23] T. B. Saw, A. Doostmohammadi, V. Nier, L. Kocgozlu, S. Thampi, Y. Toyama, P. Marcq, C. T. Lim, J. M. Yeomans, and B. Ladoux, Topological defects in epithelia govern cell death and extrusion, *Nature* **544**, 212–216 (2017).
- [24] K. Kawaguchi, R. Kageyama, and M. Sano, Topological defects control collective dynamics in neural progenitor cell cultures, *Nature* **545**, 327 (2017).
- [25] Y. Maroudas-Sacks, L. Garion, L. Shani-Zerbib, A. Livshits, E. Braun, and K. Keren, Topological defects in the nematic order of actin fibres as organization centres of hydra morphogenesis, *Nature Physics* **17**, 251–259 (2021).
- [26] P. Guillamat, C. Blanch-Mercader, G. Pernollet, K. Kruse, and A. Roux, Integer topological defects organize stresses driving tissue morphogenesis, *Nature Materials* **21**, 588–597 (2022).
- [27] K. Kruse, J. F. Joanny, F. Jülicher, J. Prost, and K. Sekimoto, Asters, vortices, and rotating spirals in active gels of polar filaments, *Physical Review Letters* **92**, 10.1103/physrevlett.92.078101 (2004).
- [28] R. Voituriez, J. F. Joanny, and J. Prost, Spontaneous flow transition in active polar gels, *Europhysics Letters (EPL)* **70**, 404–410 (2005).
- [29] G. Duclos, C. Blanch-Mercader, V. Yashunsky, G. Salbreux, J.-F. Joanny, J. Prost, and P. Silberzan, Spontaneous shear flow in confined cellular nematics, *Nature Physics* **14**, 728–732 (2018).
- [30] C. Blanch-Mercader, P. Guillamat, A. Roux, and K. Kruse, Quantifying material properties of cell monolayers by analyzing integer topological defects, *Physical Review Letters* **126**, 10.1103/physrevlett.126.028101 (2021).
- [31] A. Opatthalage, M. M. Norton, M. P. N. Juniper, B. Langeslay, S. A. Aghvami, S. Fraden, and Z. Dogic, Self-organized dynamics and the transition to turbulence of confined active nematics, *Proceedings of the National Academy of Sciences* **116**, 4788–4797 (2019).
- [32] R. Alert, J.-F. Joanny, and J. Casademunt, Universal scaling of active nematic turbulence, *Nature Physics* **16**, 682 (2020).
- [33] D. Marenduzzo, E. Orlandini, M. E. Cates, and J. M. Yeomans, Steady-state hydrodynamic instabilities of ac-

- tive liquid crystals: Hybrid lattice boltzmann simulations, *Physical Review E* **76**, 10.1103/physreve.76.031921 (2007).
- [34] T. N. Shendruk and J. M. Yeomans, Multi-particle collision dynamics algorithm for nematic fluids, *Soft Matter* **11**, 5101–5110 (2015).
- [35] M. Varghese, A. Baskaran, M. F. Hagan, and A. Baskaran, Confinement-induced self-pumping in 3d active fluids, *Physical Review Letters* **125**, 10.1103/physrevlett.125.268003 (2020).
- [36] T. Kozhukhov and T. N. Shendruk, Mesoscopic simulations of active nematics, *Science Advances* **8**, 10.1126/sciadv.abo5788 (2022).
- [37] L. Metselaar, J. M. Yeomans, and A. Doostmohammadi, Topology and morphology of self-deforming active shells, *Physical Review Letters* **123**, 10.1103/physrevlett.123.208001 (2019).
- [38] S. C. Al-Izzi and R. G. Morris, Morphodynamics of active nematic fluid surfaces, *Journal of Fluid Mechanics* **957**, 10.1017/jfm.2023.18 (2023).
- [39] I. Nitschke and A. Voigt, Active nematodynamics on deformable surfaces (2024).
- [40] T. Vicsek, A. Czirók, E. Ben-Jacob, I. Cohen, and O. Shochet, Novel type of phase transition in a system of self-driven particles, *Physical Review Letters* **75**, 1226–1229 (1995).
- [41] M. Basan, J. Prost, J.-F. Joanny, and J. Elgeti, Dissipative particle dynamics simulations for biological tissues: rheology and competition, *Physical Biology* **8**, 026014 (2011).
- [42] M. Bär, R. Großmann, S. Heidenreich, and F. Peruani, Self-propelled rods: Insights and perspectives for active matter, *Annual Review of Condensed Matter Physics* **11**, 441 (2020).
- [43] H. Chaté, Dry aligning dilute active matter, *Annual Review of Condensed Matter Physics* **11**, 189–212 (2020).
- [44] O. Hallatschek, S. S. Datta, K. Drescher, J. Dunkel, J. Elgeti, B. Waclaw, and N. S. Wingreen, Proliferating active matter, *Nature Reviews Physics* **5**, 407–419 (2023).
- [45] J. Ranft, M. Basan, J. Elgeti, J.-F. Joanny, J. Prost, and F. Jülicher, Fluidization of tissues by cell division and apoptosis, *Proceedings of the National Academy of Sciences* **107**, 20863 (2010).
- [46] N. Podewitz, M. Delarue, and J. Elgeti, Tissue homeostasis: A tensile state, *Europhysics Letters* **109**, 58005 (2015).
- [47] M. Basan, J. Elgeti, E. Hannezo, W.-J. Rappel, and H. Levine, Alignment of cellular motility forces with tissue flow as a mechanism for efficient wound healing, *Proceedings of the National Academy of Sciences* **110**, 2452 (2013).
- [48] A.-K. Marel, N. Podewitz, M. Zorn, J. O. Rädler, and J. Elgeti, Alignment of cell division axes in directed epithelial cell migration, *New Journal of Physics* **16**, 115005 (2014).
- [49] R. D. Groot and P. B. Warren, Dissipative particle dynamics: Bridging the gap between atomistic and mesoscopic simulation, *The Journal of Chemical Physics* **107**, 4423–4435 (1997).
- [50] P. Nikunen, M. Karttunen, and I. Vattulainen, How would you integrate the equations of motion in dissipative particle dynamics simulations?, *Computer Physics Communications* **153**, 407–423 (2003).
- [51] Supplementary material, URL_will_be_inserted_by_publisher, contents: A. , B., C., D.
- [52] X. Tang and J. V. Selinger, Theory of defect motion in 2d passive and active nematic liquid crystals, *Soft Matter* **15**, 587–601 (2019).
- [53] L. Onsager, The effects of shape on the interaction of colloidal particles, *Annals of the New York Academy of Sciences* **51**, 627–659 (1949).
- [54] W. Maier and A. Saupe, Eine einfache molekulare theorie des nematischen kristallinflüssigen zustandes, *Zeitschrift für Naturforschung A* **13**, 564–566 (1958).
- [55] L. Giomi, L. Mahadevan, B. Chakraborty, and M. F. Hagan, Excitable patterns in active nematics, *Physical review letters* **106**, 218101 (2011).
- [56] S. P. Thampi, R. Golestanian, and J. M. Yeomans, Vorticity, defects and correlations in active turbulence, *Philosophical Transactions of the Royal Society A: Mathematical, Physical and Engineering Sciences* **372**, 20130366 (2014).
- [57] S. P. Thampi, R. Golestanian, and J. M. Yeomans, Velocity correlations in an active nematic, *Physical Review Letters* **111**, 10.1103/physrevlett.111.118101 (2013).
- [58] L. Pismen, Dynamics of defects in an active nematic layer, *Physical Review E—Statistical, Nonlinear, and Soft Matter Physics* **88**, 050502 (2013).
- [59] L. Giomi, M. J. Bowick, X. Ma, and M. C. Marchetti, Defect annihilation and proliferation in active nematics, *Physical review letters* **110**, 228101 (2013).
- [60] L. Giomi, M. J. Bowick, P. Mishra, R. Sknepnek, and M. Cristina Marchetti, Defect dynamics in active nematics, *Philosophical Transactions of the Royal Society A: Mathematical, Physical and Engineering Sciences* **372**, 20130365 (2014).
- [61] L. Brézin, T. Risler, and J.-F. Joanny, Spontaneous flow created by active topological defects, *The European Physical Journal E* **45**, 30 (2022).
- [62] M. R. Shaebani, A. Wysocki, R. G. Winkler, G. Gompfer, and H. Rieger, Computational models for active matter, *Nature Reviews Physics* **2**, 181 (2020).
- [63] J. Elgeti, M. Cates, and D. Marenduzzo, Defect hydrodynamics in 2d polar active fluids, *Soft Matter* **7**, 3177 (2011).
- [64] F. Montel, M. Delarue, J. Elgeti, L. Malaquin, M. Basan, T. Risler, B. Cabane, D. Vignjevic, J. Prost, G. Cappello, *et al.*, Forcing tumor arrest news in ophthalmology: Viewpoint: Forcing tumor arrest viewpoint: Forcing tumor arrest, *Phys. Rev. Lett* **107**, 188102 (2011).
- [65] F. Montel, M. Delarue, J. Elgeti, D. Vignjevic, G. Cappello, J. Prost, and J.-F. Joanny, Stress clamp experiments on multicellular tumor spheroids, *Biophysical Journal* **102**, 220a (2012).
- [66] M. Delarue, F. Montel, O. Caen, J. Elgeti, J.-M. Siaugue, D. Vignjevic, J. Prost, J.-F. Joanny, and G. Cappello, Mechanical control of cell flow in multicellular spheroids, *Physical review letters* **110**, 138103 (2013).
- [67] M. P. Allen and D. J. Tildesley, *Computer Simulation of Liquids* (Oxford University Press/Oxford, 2017).

S1. PASSIVE NEMATIC FLUID (2D)

Here we consider a two dimensional passive system with channel geometry along the x -direction, as described in Fig. 2 of the main text for $v_a = 0$. We vary the packing fraction pf and temperature $k_B T$, Fig. S1. Note that for a fixed value of N_p , packing fraction pf and agent density N/Ω are equivalent. Here the initial distribution of orientations for agents is horizontal.

First, we compute the global nematic order S (see Methods) on Fig. S1b. At low temperature, a high packing fraction induces a large nematic order [53], Fig. S1c, whereas the nematic order remains small for low pf Fig. S1a. At larger temperature, fluctuations are too large to maintain agent-agent alignment and nematic order decreases [54]. Thus, the parameters chosen in the main text, $k_B T = 0.1$ and $pf = 0.8$ correspond to a regime of high nematic order.

To ensure that a high nematic order corresponds to a nematic phase, we compute the mean square displacement (MSD) of agents as a function of packing fraction for temperature $k_B T = 0.1$, Fig. S1d. At long times, the MSD is diffusive (linear in time), and becomes larger than the squared agent length over a characteristic time smaller than the simulation time. This indicates that neighbor exchange events occur, as expected in a liquid phase. Note that for temperatures smaller than $k_B T = 0.1$, the dynamics progressively becomes jammed (data not shown), and we chose parameters to avoid this solid-like phase.

In addition, we compute the auto-correlation functions (ACF) for orientation, \tilde{C}_{uu} , and velocity, \tilde{C}_{vv} , using from agents α their orientation $\hat{\mathbf{u}}_\alpha$ and velocity \mathbf{v}_α (see methods). The orientation ACF relaxes approximately to S^2 at equilibrium [REF], and Fig. S1e confirms that nematic order increases with pf . The relaxation time to a steady-state value occurs over a characteristic time $\tau_u \approx 150$, significantly smaller than the total simulation time. In addition, velocity ACF shows an exponential relaxation of velocity correlations Fig. S1f,i, over a characteristic time $\tau_v \approx 20$.

Thus, we confirm that the parameters $pf = 0.8$ and $T_n = 0.1$ in the main text correspond to a nematic-like phase. The equilibrium properties of the passive nematic fluid described here can be probed over simulation times much longer than τ_u and τ_v , hence the choice $t_{\text{sim}} \geq 5000$ in the main text or $t_{\text{sim}} = 2000$ here.

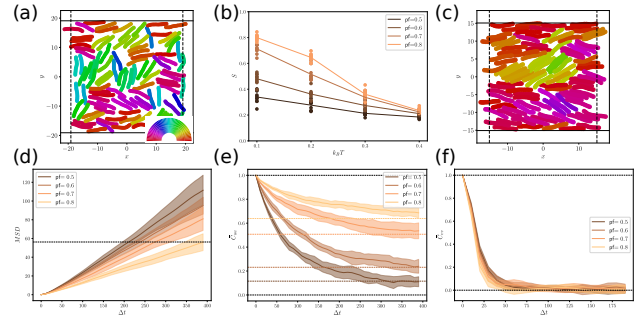


Figure S1. *Supplementary results for a passive system in channel geometry, with $N_p = 14$, $N = 100$, $t_{\text{sim}} = 2000$.* (a,c): Snapshot of the system at last simulation time point $t = 2000$, for $pf = 0.5$ (a) or $pf = 0.8$ (c) with $k_B T = 0.1$. Agents are colored depending on their orientation, see the inset in (a) for the nematic color wheel. (b): Global nematic order S as a function of temperature $k_B T$ and packing fraction pf . Dots represent time-averaged S from each simulation. (d-f): Agent mean-square displacement MSD (d), agent orientation auto-correlation function (ACF) C_{uu} (e) and agent velocity ACF C_{vv} (f) as a function of time difference Δt , varying pf at fixed $k_B T = 0.1$. The dashed line on (d) indicates the square of the agent length $l_a = r_0(N_p - 1) + r_c$. The color dashed lines on (e) indicate average S^2 values for each condition.

Averages are performed over $N_{\text{sim}} = 10$ independent simulations, with $N_b = 4$ time blocks for MSD and orientational ACF, and $N_b = 9$ time blocks for velocity ACF. Averages are indicated by full lines (b,d,e,f), and filled regions represent deviations from the mean of one standard error (d-f).

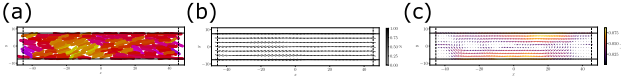


Figure S2. *Narrow channel width as a function of activity.* (a-c): Snapshots of particle positions (a), nematic field (b) and velocity field (c) at $v_a = -3$. Parameters $N = 30 \times 5$ and $N_p = 14$, simulation time $t_{\text{sim}} = 5000$, $N_{\text{sim}} = 10$ independent simulations per condition.

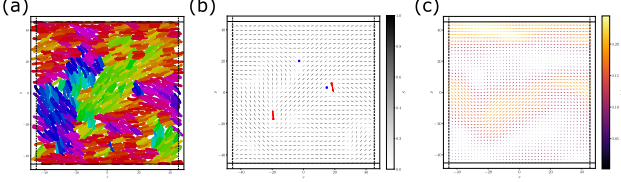


Figure S3. *Large channel width as a function of activity.* (a-c): Snapshots of particle positions (a), nematic field (b) and velocity field (c) at $v_a = -3$. Parameters $N = 30 \times 30$ and $N_p = 14$, simulation time $t_{\text{sim}} = 5000$, $N_{\text{sim}} = 10$ independent simulations per condition.

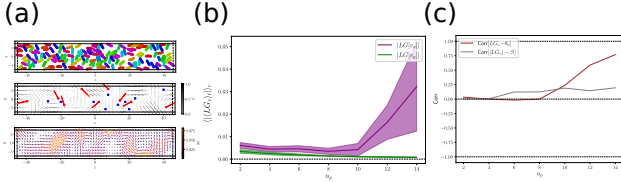


Figure S4. *Narrow channel width as a function of the number of particles per agent N_p .* (a): Snapshot of the particle positions (top), velocity field (middle) and nematic field (bottom) at $N_p = 6$. (b): Change of the maximal mode amplitude of velocity Fourier-Legendre projection $\text{LG}[\mathbf{v}]$ as a function of the number of particles per agent. (c): Correlation plot between the velocity magnitude $|\text{LG}_v|$ and nematic order S (gray), or between the velocity LG_v and director angle θ_n (red), for a change of the number of particles per agent. Parameters $N = 30 \times 5$ and $N_p = 14$, simulation time $t_{\text{sim}} = 5000$, $N_{\text{sim}} = 10$ independent simulations per condition.

S2. SUPPLEMENTARY RESULTS

Here we detail supplementary results for Fig. 2 in the main text, Figs. S2-4, and supplementary results for Fig. 3,4 in the main text, Fig. S5.

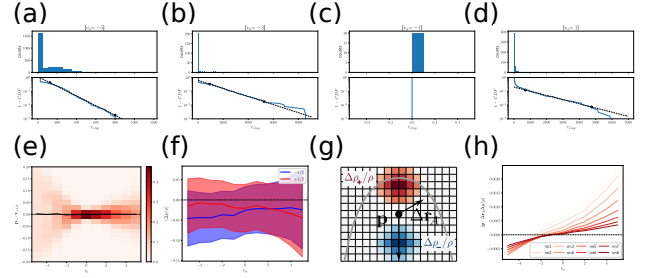


Figure S5. *Active system with PBCs and $pc = 14$, $N = 400$, $N_{\text{sim}} = 20$.* (a,d): Histogram of the distribution of switching times for $|\theta_v| > \pi/4$ (top), and reciprocal cumulative distribution function (CDF) in log-space (bottom). The black dots represent the time interval over which the exponential fit is performed, indicated by a dashed line. (e): Density histogram as a function of activity of the $+1/2$ -defect core velocity $\mathbf{v}_{+1/2}$ projected in the direction perpendicular to the defect polarity, $\hat{\mathbf{p}}_{\perp} = (-\sin \theta_p, \cos \theta_p)$. (f): Instantaneous correlation between defect position $\mathbf{r}_{\pm 1/2}$ and relative density $\Delta \rho / \rho$. (g): Sketch for the definition of the density dipole $D_{\rho,+1/2}$. The black dot indicates the defect center $\mathbf{r}_{+1/2}$ and defines a displacement vector $\Delta \mathbf{r}_A = \mathbf{r}_A - \mathbf{r}_{+1/2}$ around a square patch A centered at $\mathbf{r}_{1/2}$. One defines the density dipole as $D_{+1/2} = \langle (\hat{\mathbf{p}} \cdot \Delta \hat{\mathbf{r}}_A) \Delta \hat{\rho} \rangle_A$ with $\Delta \hat{\mathbf{r}}_A = \Delta \mathbf{r}_A / |\Delta \mathbf{r}_A|$. The square patch $A = L^2$ has a length $L = 2nn + 1$ in pixel units defined by coarse-grained fields, with $nn \geq 1$. (h): Average density dipole at sites of $+1/2$ -defects as a function of activity, for different next-neighbor patches with area $A = (2nn + 1)^2$ (g).

S3. PROGRAM METHODS

A. Parameter values

The parameters are

- geometric: particles per agent N_p , pair potential range r_c , bond length ℓ_0 ,
- kinetic: mass m , temperature $k_B T$,
- dissipative: ξ_s (shape), ξ_i (inter-agent), ξ_e (external substrate),
- conservative: link stiffness K_l , bending rigidity κ_b , repulsive coefficient f_0 , attractive coefficient f_1 ,
- active: active internal flow v_a .

Note that the bending rigidity κ_b of a flexible chain is often written as a function of a persistence length l_p such that $\kappa_b = k_B T l_p$. We then have $l_p = 50$ for $\kappa_b = 5$ and $k_B T = 0.1$, to be compared with agent length $l_\alpha = 7.5$ for $N_p = 14$ and $\ell_0 = 0.5$ (see below for definition of l_α).

The various interactions define under-damped characteristic times: relaxational $t_s = m/\xi_s = 0.05$,

B. Algorithmic program structure

To describe an evolving tissue with potential divisions and deaths, one uses fixed arrays for the 9 particle variables $\{r_{p,i}\}$, $\{v_{p,i}\}$, $\{F_{p,i}\}$ with spatial components i , of respective sizes $N_p \cdot N_{\max}$ determined by the expected maximal number of agents N_{\max} . The later can be easily determined from the system size Ω in the large packing limit with balls of radius $r_c/2$ and d -dimensional volume $V_d(r_c)$: $N_p \cdot N_{\max} \sim \Omega/V_d(r_c)$. The advantage of fixed arrays is to avoid the computational costs of dynamic reallocation (vectors), which becomes important when turnover is allowed.

Each array is then composed of the dynamic variables of living agents and irrelevant data for empty slots (voids). One constructs a STATUS array of size N_{\max} and indices $s = [0, N_{\max} - 1]$ to assign -1 to living agents, and the memory position of the previous void otherwise. This generates a linked list structure of voids in STATUS, thanks to a variable (head) which contains the memory position of the first void in STATUS, such that $s_1 = \text{STATUS}[\text{head}]$ gives the next one, $s_2 = \text{STATUS}[s_1]$, etc..., until $\text{STATUS}[s_n] = -1$ terminates the list of voids. This structure allows to add voids to the linked list when an agent is removed, or to fill head voids with new agents when division occurs. See [REF] below for detailed description.

After initialisation of arrays $\{r_{p,i}\}$, $\{v_{p,i}\}$ for a given number of agents, one computes all the forces $\{F_{p,i}\}$ and starts the temporal evolution. This uses a modified velocity-Verlet algorithm [REF], which accounts for the velocity dependence of forces due to the dissipative interaction. From a time t to a time $t + \delta t$, one updates

$t_i = m/\xi_i \simeq 0.03$ or vibrational $T_b = \sqrt{m/K_b} \simeq 0.2$, $T_l = \sqrt{m/K_l} \simeq 0.2$, $T_g = \sqrt{m/K_g} \simeq 0.3$, $T_i = \sqrt{m/K_0} \simeq 0.6$ and $T_a = \sqrt{m/K_a}$.

This is associated with characteristic stiffnesses (force/length) $K_b = \kappa_b/\ell_0^3 = 40$, $K_l = 20$, $K_g = f_g/\ell_0 = 10$, $K_0 = f_0/r_c = 2.4$, $K_a = \xi_i \text{Max}[v_a]/r_c = 200$. Then, the corresponding over-damped characteristic times are $\tau_b = \xi_s/K_b \simeq 0.5$, $\tau_l = \xi_s/K_l = 1$, $\tau_g = \xi_s/K_g \simeq 2$, $\tau_i = \xi_i/K_0 \simeq 17$ and $\tau_a = \xi_i/K_a \simeq 0.2$. Under-damped time scales should be smaller than over-damped time scales to have large scale properties independent from inertial effects. One only needs $T/\tau = \sqrt{mK}/\xi \ll 1$ because $t/\tau = mK/\xi^2 = (T/\tau)^2$, and one gets

- $T_b/\tau_b = \sqrt{mK_b}/\xi_s \simeq 0.3$,
- $T_l/\tau_l = \sqrt{mK_l}/\xi_s \simeq 0.2$,
- $T_g/\tau_g = \sqrt{mK_g}/\xi_s \simeq 0.2$,
- $T_i/\tau_i = \sqrt{mK_0}/\xi_i \simeq 0.04$,
- $T_a/\tau_a = \sqrt{mK_a}/\xi_i \simeq 0.4$.

variables as

$$\begin{aligned}
 \mathbf{v}_p(t + \delta t/2) &= \mathbf{v}_p(t) + \frac{\delta t}{2} \mathbf{F}_p(t) \\
 \mathbf{r}_p(t + \delta t) &= \mathbf{r}_p(t) + \delta t \mathbf{v}_p(t + \delta t/2) \\
 &= \mathbf{r}_p(t) + \delta t \mathbf{v}_p(t) + \frac{\delta t^2}{2} \mathbf{F}_p(t) \\
 &\rightarrow [\text{division and/or death algorithms}] \\
 \mathbf{F}_p^{(c,r)}(t + \delta t) &= \mathbf{F}_p^{(c,r)}[\mathbf{r}(t + \delta t)] \\
 \mathbf{F}_p^{(d)}(t + \delta t) &= \mathbf{F}_p^{(d)}[\mathbf{r}(t + \delta t), \mathbf{v}_p(t + \delta t/2)] \\
 \bar{\mathbf{v}}_p(t + \delta t) &= \mathbf{v}_p(t + \delta t/2) + \frac{\delta t}{2} \mathbf{F}_p^{(c,r)}(t + \delta t) \\
 &= \mathbf{v}_p(t) + \frac{\delta t}{2} [\mathbf{F}_p(t) + \mathbf{F}_p^{(c,r)}(t + \delta t)] \\
 &\rightarrow [\text{iterative loop on } \mathbf{v}_p \text{ and } \mathbf{F}_p^{(d)} \text{ at } t + \delta t] \\
 \mathbf{v}_p(t + \delta t) &= \bar{\mathbf{v}}_p(t + \delta t) + \frac{\delta t}{2} \mathbf{F}_p^{(d)}(t + \delta t) \\
 \mathbf{F}_p^{(d)}(t + \delta t) &= \mathbf{F}_p^{(d)}[\mathbf{r}(t + \delta t), \mathbf{v}(t + \delta t)] \tag{S10}
 \end{aligned}$$

where $\mathbf{F}_p = \mathbf{F}_p^{(c)} + \mathbf{F}_p^{(d)} + \mathbf{F}_p^{(r)}$ and $\mathbf{F}_p^{(c,r)} = \mathbf{F}_p^{(c)} + \mathbf{F}_p^{(r)}$.

C. Boundary types

The code is written to account for different boundary types along each dimension: periodic, confining, absorbing or free. Confinement is implemented with a soft (quadratic) potential, and absorption deletes agents when their center-of-mass crosses the boundary. Then, one constructs the respective index $bc_i = 0, 1, 2, 3$ for each dimension i , corresponding respectively to periodic, confining, absorbing, free, and build a global index

Table I. List of parameter values used in the simulations. Parameters with symbols in parenthesis are only present for a proliferating material. Varied parameters have their values indicated under square brackets. The units are chosen so that $m = r_c = 1$ and $\delta t = 10^{-3}$.

Parameter	Value	Description
N_{sim}	[10, 20]	number of simulations per condition
δt	10^{-3}	time step
t_{sim}	[5000, 20000]	simulation time
(k_a)	0.1	rate of agent death
N_p	14	particles per agent
pf	0.8	2D packing fraction
N	[400, 450, 2500]	number of agents in 2D
r_c	1	pair potential range
ℓ_0	0.5	shape link length
(ℓ_d)	$1.5 \ell_0 (N_p - 1)$	division length threshold
(u_d)	0.1	daughter particle displacement
m	1	particle mass
K_l	20	shape link stiffness
K_w	20	external wall stiffness
κ_b	5	shape bending rigidity
(f_g)	5	shape division growth force
f_0	2.4	inter-agent repulsive coefficient
f_1	0.5	inter-agent attractive coefficient
v_a	[-5 : 5]	active flow amplitude
ξ_s	[5, 20]	shape dissipative coefficient
ξ_i	[10, 40]	inter-agent dissipative coefficient
(ξ_c)	0	external (substrate) dissipative coefficient
$k_B T$	0.1	temperature (noise)

$bc \leftrightarrow \mathbf{bc} = (bc_x, bc_y, \dots)$. In $d = 3$ dimensions, one gets $4^d = 64$ possibilities with $bc = bc_y + 4bc_x + 16bc_z$. The results presented in the main text for 2D ($bc_z = 0$) correspond to $bc = 0$ (periodic in x and y directions), $bc = 1$ (periodic in x , confining in y) and $bc = 10$ (circular absorbing). In 3D, walls along y, z and periodicity along x , or $\mathbf{bc} = (0, 1, 1)$, gives a global index $bc = 17$.

For a confining wall at $y_w = \pm W/2$, one applies a soft potential $V_w(y) = \frac{1}{2}K_w(y \pm d - y_w)^2$ and $V_w(y) = 0$ when $y < y_w - d$ or $y > y_w + d$, with force $\mathbf{F}_w(y) = -\partial V_w / \partial \mathbf{r}$. Similarly for a confining disc at $r_w = R$, one uses $V_w(r) = \frac{1}{2}K_w[r + d - R]^2$. The parameter $d = r_c/4$ is a penetration length inside the channel over which the wall potential is non-zero.

D. Neighbour list algorithm

The calculation of inter-agent particle forces requires $\mathcal{O}(N_{\text{tot}}^2)$ loop calculations per time step for N_{tot} particles. For elongated agents ($N_p \sim 10$), this scaling becomes quickly inefficient as N increases to few hundreds. Instead, one obtains a $\mathcal{O}(N_{\text{tot}})$ scaling by the use of a neighbour list algorithm [67].

It consists in dividing the available space into N_b regular boxes with $N_b = N_{bx} \cdot N_{by} \cdot N_{bz}$, and assign each particle to a box. Each box of indices (b_x, b_y, b_z) is assigned to a unique index $b = b_x + b_y \cdot N_{bx} + b_z \cdot N_{bx} \cdot N_{by} = [0, N_b - 1]$ with $b_i = [0, N_{bi} - 1]$. In 2D, one fixes $N_{bz} = 1$ and $b_z = 0$. The size r_b of boxes is chosen to be $r_b \sim r_c = 1.2 r_c$ so that one only needs to loop over nearest neighbour boxes when calculating inter-agent interactions. Since the list of particles for each box is evolving at each time, the best algorithmic structure for this purpose is a linked list.

For each box of index b , the memory index $p = [0, N_{\text{tot}}]$ of the first particle found is assigned to the entry $\text{HEAD}[b] = p$ of a HEAD list of size N_b . If the box remains empty, $\text{HEAD}[b] = -1$. The next particle p' found in the box is linked to the previous one with a LINK list of size N_{tot} , initialized to $\text{LINK}[p] = -1$, so that $\text{LINK}[p'] = \text{HEAD}[b]$. This particle becomes the new head of the list hence $\text{HEAD}[b] = p'$. By repetition, this creates a linked list of particles $q = \text{LINK}[p]$ belonging to each box b , starting from the head particle $p_{\text{head}} = \text{HEAD}[b]$. The linkage terminates when $\text{LINK}[p] = -1$.

One needs to reconstruct this linked structure at every time step ($\mathcal{O}(N_{\text{tot}})$), but the inter-agent interactions are

now performed in a loop over boxes with $\mathcal{O}(N_b nn)$ where the number of neighbour boxes is $nn \sim 3^d/2$. The factor of 2 is due to adjacent boxes sharing neighbours, so that one can only loop over half of them for each box (usually upper-right corner). Since $N_b \sim N_{\text{tot}}$ because $r_b \sim r_c$, one replaces a double loop of scaling $\mathcal{O}(N_{\text{tot}}^2)$ by two loops of scaling $\mathcal{O}(N_{\text{tot}})$, one for generating the linked list and one for computing interaction forces.

To identify neighbour boxes, one needs to be careful about boundary conditions. Boxes are defined on the system's volume Ω , such that $N_{b,k} = \text{floor}(L_{b,k}/r_b)$ with $L_{b,k} = L_k$ and $r_{b,k} = L_{b,k}/N_{b,k}$. In case of soft confinement or absorbing conditions, particles can exist away from the defined system's volume and one must increase $\{L_{b,k}\}$ accordingly to ensure that all particles are assigned to a box. Next, one adds an extra layer called ghost boxes, which link the boxes from opposite sides in case of periodic boxes and are empty otherwise. Ghost boxes serve to define a unique displacement map from a box to its neighbour boxes. For instance in 2D, a box $\mathbf{b} = (b_x, b_y)$ has 4 independent neighbours $\mathbf{b} + \Delta$, where $\Delta_x = \{1, 1, 1, 0\}$ and $\Delta_y = \{-1, 0, 1, 1\}$ link \mathbf{b} to the upper-right corner of nearest neighbours (starting from lower right neighbour box).

E. Initial configuration

The large aspect ratio of agents requires care for the initial preparation of the system when $N_c(t_i) > 1$, to avoid agent overlap. Each agent's center-of-mass is assigned a position on a regular grid of length steps $\{a_k\}$ in each direction k , such that $a_k = L_k/N_k$. The position is $r_{k,f} = -L_k/2 + a_k \cdot (f+1/2)$ with $-L_k/2 < r_k < L_k/2$ for $f = [0, N_k - 1]$. We prepare the system into either isotropic or nematic states.

For an isotropic state, agent orientation $\hat{\mathbf{u}}_\alpha = (\sin \theta_\alpha \cos \phi_\alpha, \sin \theta_\alpha \sin \phi_\alpha, \cos \theta_\alpha)$ is sampled over uniform random generators ($\phi_\alpha = 2\pi \cdot \text{rand}[0, 1]$, $\theta_\alpha = \pi \cdot \text{rand}[0, 1]$). One fixes $\theta_\alpha = \pi/2$ in two dimensions. Initial agent bond length l_{0i} is reduced to avoid particle collisions, such that the agent length satisfies $l_{0i} \cdot (N_p - 1) < \min(\{a_k\})$.

For a nematic state, its direction is set as $\hat{\mathbf{n}} = (\sin \theta_n \cos \phi_n, \sin \theta_n \sin \phi_n, \cos \theta_n)$. We only consider nematic directions $\hat{\mathbf{e}}_x$, $\hat{\mathbf{e}}_y$ or $\hat{\mathbf{e}}_z$ for simplicity. Here agents are placed on the defined grid, but shifted alternatively in a chosen orthogonal direction $\hat{\mathbf{n}}_\perp$ by an amount $\pm a_\perp/4$. Thus for agent indices α along the nematic direction and α_\perp perpendicular to the plane containing $\hat{\mathbf{n}}, \hat{\mathbf{n}}_\perp$ (in three dimensions), one writes $r_{\perp,\alpha} = r_{\perp,\alpha} + a_\perp(2\alpha \% 2 - 1)(2\alpha_\perp \% 2 - 1)/4$ where $\%$ is the modulo operation. For elongated agents, the effective transverse spacing is then $a_\perp/2$, and one chooses the initial bond length l_{0i} such that $2a_\parallel - l_{0i} \cdot (N_p - 1) \sim a_\parallel/2$ to have similar agent spacing in the longitudinal direction. This choice has the advantage to reduce the need of initial compaction, and also to start the simulation from a non-crystallized

structure. The orientation of each agent $\hat{\mathbf{u}}_\alpha$ follows $\phi_\alpha = \phi_n + \Delta\phi \cdot \text{rand}[-1, 1]$, $\theta_\alpha = \theta_n + \Delta\theta \cdot \text{rand}[-1, 1]$ where $\Delta\theta = \Delta\phi = 0.1$.

After the generation of particle positions, one creates the LINK list for the neighbour list algorithm (see above).

In addition, one assigns for each particle and each spatial component i an initial velocity $v_{p,i} = \sqrt{T_n/m} \cdot \mathcal{N}(0, 1)$, where $\mathcal{N}(0, 1)$ is a random variable distributed over a normalised centered Gaussian. This means that the initial velocity distribution is Maxwell-Boltzmann and satisfies the equipartition theorem. The net linear momentum per particle is then calculated and subtracted from each $v_{p,i}$ to start with a global system at rest.

F. Effective aspect ratio and packing fraction

Instead of fixing the number density of agents, we estimate the effective d -dimensional volume $V_\alpha^{(d)}$ occupied by a agent and fix a packing fraction $\text{pf} = N V_\alpha / \Omega$ where Ω is the system's volume.

Because of the contact interaction limited by the cut-off range r_c , agents can be represented as spherocylinders (circo-rectangles in two dimensions) of width r_c , and length $l_\alpha = (N_p - 1)\ell_0 + r_c$. This allows to define an effective aspect ratio of agents $\text{ar} = l_\alpha / r_c = 1 + (N_p - 1)\ell_0 / r_c$. The limit of a unit aspect ratio corresponds to a sphere (circle) with $N_p = 2$ and $\ell_0 = 0$.

The agent volume is then $V_\alpha^{(3)} = \frac{4\pi}{3}(r_c/2)^3 + \pi(r_c/2)^2(N_p - 1)\ell_0$ in three dimensions, and $V_\alpha^{(2)} = \pi(r_c/2)^2 + r_c(N_p - 1)\ell_0$ in two dimensions. One then chooses the number of agents N and packing fraction pf for a simulation, and determines the system's size $L = \Omega^{1/d} = (N V_\alpha / \text{pf})^{1/d}$. To obtain different sizes in different spatial directions i, j , one chooses the individual number of agents per dimension $\{N_k\}_{k=1}^d$ such that $N = \prod_{k=1}^d N_k$. Then, one computes the system's length in a direction i with $L_i = N_i (V_\alpha / \text{pf})^{1/d}$ whereas other directions $j \neq i$ have sizes $L_j = (N_j / N_i) L_i$. This ensures that $\Omega = \prod_{k=1}^d L_k = N V_\alpha / \text{pf}$.

Alternatively, to reach nematic order in three dimensions, one can start from the two dimensional packing fraction $\text{pf}^{(2)} = N_\parallel N_\perp V_\alpha^{(2)} / (L_\parallel L_\perp)$ in the plane containing $\hat{\mathbf{n}}, \hat{\mathbf{n}}_\perp$, with $N = N_\parallel N_\perp N_{\perp\perp}$ and $\Omega = L_\parallel L_\perp L_{\perp\perp}$ (see previous section on nematic intialization). To ensure that inter-agent distances are similar in the two directions perpendicular to the nematic direction, one imposes a transverse inter-agent distance $a_{\perp\perp} = a_\perp/2$ and define $L_{\perp\perp} = N_{\perp\perp} a_{\perp\perp} = (N_{\perp\perp} / N_\perp) L_\perp$. Calling v the dimensionless ratio of volumes $v = 2V_\alpha^{(3)} / [V_\alpha^{(2)}]^{3/2}$, the 3D packing fraction is written as $\text{pf}^{(3)} = N V_\alpha^{(3)} / \Omega = v [\text{pf}^{(2)}]^{3/2}$. For the chosen parameters $\text{pf}^{(2)}$, r_c , N_p and ℓ_0 , one gets $v \simeq 0.57$ and $\text{pf}^{(3)} \simeq 0.41$.

G. Division and Death

Division of agents is introduced by adding a constant growth force f_g to the shape link force $F^{(1)}(r) = K_l(\ell_0 - r) + f_g$. This defines an effective link length $\ell_{0g} = \ell_0 + f_g/K_l$ and one triggers division when the agent size $\ell_{0g} \cdot (N_p - 1)$ reaches a critical size ℓ_d such that $\ell_0 \cdot (N_p - 1) < \ell_d < \ell_{0g} \cdot (N_p - 1)$. For an elongated agent of axis $\hat{\mathbf{n}}_\alpha$, division can be performed transversely to the agent axis or longitudinally, and we choose the later case here.

The first case means creating clones of all particles $p = [0, N_p - 1]$ of the "mother" agent and applying displacements $\Delta \mathbf{r} = \pm u_d \hat{\mathbf{n}}_{\perp, \alpha}$ to the "daughter" agent particles with $u_d \ll \ell_0$. In memory, one simply needs to copy p into a new slot, given by the first void (head) in the linked list of STATUS. Then the next void STATUS[head] = newhead becomes the new head and STATUS[head] is assigned -1 because the "daughter" agent is alive.

The second case means to separate the agent with particles $p = [0, N_p - 1]$ into two "daughter" agents with particles $p_1 = [0, N_p/2 - 1]$, $p_2 = [N_p/2, N_p - 1]$, and cloning all particles. In memory, one replaces the p -allocations by p_1 and copies p_2 into a new slot. New particles are assigned a fixed displacement along the agent axis $\Delta \mathbf{r} = \pm u_d \hat{\mathbf{n}}_\alpha$, forward for p_1 and backward for p_2 to ensure a bijective relation between spatial organization and memory allocation.

In our simulations, we choose to use the algorithm for longitudinal division. Note that both cases preserve the local nematic order of agents.

If allowed in the program, agent death (akin to cell apoptosis) is tested for each agent at each time step, and done if a random variable $r = \text{rand}[0, 1]$ satisfies $r < k_a \delta t$, where k_a is the apoptotic rate and δt the time step. The agent life time is then distributed exponentially. If a living agent s with STATUS[s] = -1 is removed, this creates a new void and it is linked to previous head by STATUS[s] = head followed by head = s so that s becomes the new head void.

S4. ANALYSIS METHODS

A. Nematic order

In d spatial dimensions, the global nematic tensor \mathbf{Q} of a set of N agents with orientations $\hat{\mathbf{u}}_\alpha$ is given by

$$\mathbf{Q} = \frac{1}{N(d-1)} \sum_{\alpha=1}^N (d \hat{\mathbf{u}}_\alpha \hat{\mathbf{u}}_\alpha - \mathbf{1}) \simeq \frac{S}{d-1} (d \hat{\mathbf{n}} \hat{\mathbf{n}} - \mathbf{1}) \quad (\text{S11})$$

where S is the global nematic order and $\hat{\mathbf{n}}$ the global director. The second equality assumes a uniaxial nematic, which is expected to be a good approximation for rod-like particles in 3D, but is exact only in 2D. Operationally, $S = [0; 1]$ is the largest positive eigenvalue of \mathbf{Q} and $\hat{\mathbf{n}}$ the corresponding eigenvector. Perfect nematic order $S = 1$ is achieved when $\hat{\mathbf{u}}_\alpha = \hat{\mathbf{n}}$ for all α . From the end-to-end agent displacement $\Delta \mathbf{r}_\alpha = \mathbf{r}_\alpha[N_p - 1] - \mathbf{r}_\alpha[0]$, one defines the agent orientation $\hat{\mathbf{u}}_\alpha = \Delta \mathbf{r}_\alpha / |\Delta \mathbf{r}_\alpha|$.

In two dimensions, one can show explicitly that $S[2D] = \sqrt{(\mathbf{Q} : \mathbf{Q})/2} = \sqrt{Q_{xx}^2 + Q_{xy}^2}$ with $\hat{\mathbf{n}} = \cos \theta_n \hat{\mathbf{e}}_x + \sin \theta_n \hat{\mathbf{e}}_y$ and $\theta_n = 1/2 \arctan 2(Q_{xy}/Q_{xx})$. In 2D, the nematic tensor has two degrees of freedom $\{Q_{xx}, Q_{xy}\}$, which allows to determine exactly S and θ_n in the director representation.

In three dimensions, the nematic tensor has five degrees of freedom $\{Q_{xx}, Q_{xy}, Q_{xz}, Q_{yy}, Q_{yz}\}$ but the director representation only involves three parameters $\{S, \theta_n, \phi_n\}$ with $\hat{\mathbf{n}} = \sin \theta_n [\cos \phi_n \hat{\mathbf{e}}_x + \sin \phi_n \hat{\mathbf{e}}_y] + \cos \theta_n \hat{\mathbf{e}}_z$. This difference originates from the possibility of biaxial nematic order in 3D, with two principal directions $\hat{\mathbf{n}}_1, \hat{\mathbf{n}}_2$ with respective orders S_1 and S_2 . This gives five degrees of freedom with the orthogonality condition $\hat{\mathbf{n}}_1 \cdot \hat{\mathbf{n}}_2 = 0$. In that case, one needs to diagonalize \mathbf{Q} , and identify S as the largest positive eigenvalue of \mathbf{Q} with the corresponding eigenvector $\hat{\mathbf{n}}$. A test for biaxiality is done by comparing the second largest eigenvalue S_2 with $-S/2$. Indeed, we observe that fluctuations introduce transient ordering such that $|S_2 + S/2| \neq 0$ in average.

Similarly, one constructs a nematic tensor associated to the particle velocities $\{\mathbf{v}_p\}$, which reads in dimensional or dimensionless versions

$$\mathbf{Q}_v = \frac{1}{N_{\text{tot}}(d-1)} \sum_{p=1}^{N_{\text{tot}}} (d \mathbf{v}_p \mathbf{v}_p - |\mathbf{v}_p|^2 \mathbf{1}), \quad (\text{S12})$$

$$\hat{\mathbf{Q}}_v = \frac{1}{N_{\text{tot}}(d-1)} \sum_{p=1}^{N_{\text{tot}}} (d \hat{\mathbf{v}}_p \hat{\mathbf{v}}_p - \mathbf{1}) \quad (\text{S13})$$

where $\hat{\mathbf{v}}_p = \mathbf{v}_p / |\mathbf{v}_p|$. In two dimensions, one can write $\hat{\mathbf{Q}}_v = S_v (2 \hat{\mathbf{n}}_v \hat{\mathbf{n}}_v - \mathbf{1})$, with the velocity order parameter S_v and the corresponding velocity director $\hat{\mathbf{n}}_v$.

To eliminate the fast velocity fluctuations and focus on large scale coherent motion, one replaces in subsequent analysis the instantaneous velocities $\{\mathbf{v}_p\}$ by mean velocities $\{\bar{\mathbf{v}}_p\}$, where $\bar{\mathbf{v}}_p(t) = \mathbf{u}_p(t, \bar{\delta t}) / \bar{\delta t}$. The

temporal displacement \mathbf{u}_p is forward (backward) for the first (last) time point, and central otherwise with $\mathbf{u}_p(t, \delta t) = 1/2[\mathbf{r}_p(t + \delta t) - \mathbf{r}_p(t - \delta t)]$. One chooses $\delta t = [1000, 10000] \times \delta t = [1, 10]$ depending on the data writing frequency.

B. Coarse-grained fields

From a given configuration of particles $\{\mathbf{r}_p, \bar{\mathbf{v}}_p\}$, one builds coarse-grained spatial fields for number density $n(\mathbf{r})$, velocity $\bar{\mathbf{v}}(\mathbf{r})$ and nematic order $\mathbf{Q}(\mathbf{r})$ over a regular spatial grid of points $\{\mathbf{r}\}$. This requires the coarse-graining of microscopic distribution functions with a weight function $W(\mathbf{R})$

$$\begin{aligned} n(\mathbf{r}) &= \sum_p \delta(\mathbf{r} - \mathbf{r}_p) \rightarrow \sum_p W(\mathbf{r} - \mathbf{r}_p) \quad (\text{S14}) \\ n(\mathbf{r})\bar{\mathbf{v}}(\mathbf{r}) &= \sum_p \bar{\mathbf{v}}_p \delta(\mathbf{r} - \mathbf{r}_p) \rightarrow \sum_p \bar{\mathbf{v}}_p W(\mathbf{r} - \mathbf{r}_p) \\ n(\mathbf{r})\mathbf{Q}(\mathbf{r}) &= \sum_p \mathbf{Q}_p \delta(\mathbf{r} - \mathbf{r}_p) \rightarrow \sum_p \mathbf{Q}_p W(\mathbf{r} - \mathbf{r}_p) \\ &\simeq \frac{n(\mathbf{r})s(\mathbf{r})}{d-1} [d\hat{\mathbf{n}}(\mathbf{r})\hat{\mathbf{n}}(\mathbf{r}) - \mathbf{1}] \end{aligned}$$

The individual nematic tensor \mathbf{Q}_p is defined for each particle p belonging to an agent α as $\mathbf{Q}_p = (1/N_p)(d\hat{\mathbf{u}}_\alpha\hat{\mathbf{u}}_\alpha - \mathbf{1})/(d-1)$.

The weight function is defined such that $\int d^d\mathbf{R} W(\mathbf{R}) = 1$, and one chooses for simplicity an isotropic step function $W(R) = \text{If}[R \leq r_w, 1/V_d(r_w)], \text{Else}[0]$ parameterized by the window radius r_w and dependent on the d -sphere volume $V_d(r_w)$ of the window. The advantage of a step function compared to a smooth (gaussian) kernel is that the spatial integration of the function is not sensitive to the spatial grid resolution. Note that for non-periodic boundaries defined at spatial points $\{\mathbf{r}_b\}$, $V_d(r_w)$ depends on the distance $|\mathbf{r} - \mathbf{r}_b|$ because spatial points external to the system are excluded (precisely to avoid boundary effects). For instance at a boundary point of a flat wall, only half the volume $V_d(r_w)$, internal to the system, must be considered. This effect is captured by a simple linear scaling with the normal distance to boundary $s_n = |\mathbf{r} - \mathbf{r}_{b,n}| \leq r_w$ such that $V_d(r_w, \mathbf{r}) = V_d(r_w) \cdot \{\text{If}[s_n \leq r_w, (s_n/r_w + 1)/2], \text{Else}[1]\}$.

The window radius r_w is defined from the total number of particles N_{tot} and the system size Ω such that the window spherical volume $V_d(r_w)$ contains a certain number of particles N_w in the bulk. This imposes the relation $N_w/V_d(r_w) = N_{\text{tot}}/\Omega$. One chooses the free parameter $N_w = 112$, corresponding to 8 agents per window or $r_w \simeq 3.8r_c$ with the particle density considered in results.

C. Detection of defects in two dimensions

From the coarse-grained nematic field $\mathbf{Q}(\mathbf{r})$ and associated director field $\hat{\mathbf{n}}(\mathbf{r}) = (\cos \theta_n(\mathbf{r}), \sin \theta_n(\mathbf{r}))$, one computes the winding number field $q(\mathbf{r}) = (1/2\pi) \oint_{\mathcal{C}(\mathbf{r})} d\theta_n(\mathbf{r})$ around a closed loop $\mathcal{C}(\mathbf{r})$. We use a CCW nearest-neighbour grid contour around each spatial point \mathbf{r} , such that the displacement map from the point \mathbf{r} is $\{\mathbf{u}_c\}$ with $\{u_{c,x}\} = \Delta_x \cdot \{+, +, 0, -, -, -, 0, +, +\}$ and $\{u_{c,y}\} = \Delta_y \cdot \{0, +, +, +, 0, -, -, -, 0\}$. The winding number $q(\mathbf{r})$ is computed from an oriented integration of the director angle [REF]. Defining the contour positions as $\{\mathbf{r}_c = \mathbf{r} + \mathbf{u}_c\}$ with $c = [0, N_c]$ and $0 \equiv N_c$, one defines the angle difference $\Delta\theta_n = \theta_n(\mathbf{r}_{c+1}) - \theta_n(\mathbf{r}_c)$ for each displacement and adds up the total charge $q += (1/2\pi)[\Delta\theta_n + B(\theta_n)]$ from all c , where $B(x) = \{\text{If}[x > \pi/2, -\pi], \text{Elif}[x < -\pi/2, \pi], \text{Else}[0]\}$. Then, one applies an aggregation algorithm to merge topological defects of the same charge which are nearest neighbours on the spatial grid. Finally, the defect polarity $\hat{\mathbf{p}}$ of $+1/2$ -defects is computed using the unit nematic divergence [REF] $\hat{\mathbf{p}} = \nabla \cdot \mathbf{Q}/|\nabla \cdot \mathbf{Q}|$, with derivatives defined also from nearest neighbour differences.

For non-periodic boundaries, one cannot define a closed contour to compute a winding number. Instead, one defines a half-contour and count the number of half-rotations, so that $q += (1/\pi)[\Delta\theta_n + B(\theta_n)]$ with $\{\mathbf{u}_c\} = \pm[\Delta_x, \Delta_y] \cdot \{[+, 0], [+, +], [0, +], [-, +], [-, 0]\}$. Derivatives are also adapted near boundaries (backward/forward instead of central depending on direction) to compute the defect polarity $\hat{\mathbf{p}}$ of $+1/2$ -defects.

D. Correlation functions

In two dimensions, we compute temporal Auto-Correlation Functions (ACF) from individual agents or particles as follows,

- orientation ACF

$$\bar{C}_{uu}(\Delta t) = \langle 2[\hat{\mathbf{u}}_\alpha(t_0 + \Delta t) \cdot \hat{\mathbf{u}}_\alpha(t_0)]^2 - 1 \rangle_{\alpha, t_0}$$

- velocity ACF for particles

$$\bar{C}_{vv}^{(p)}(\Delta t) = \langle \mathbf{v}_p(t_0 + \Delta t) \cdot \mathbf{v}_p(t_0) \rangle_{p, t_0} / \langle \mathbf{v}_p^2(t) \rangle_{p, t}$$

- mean-square displacement

$$\text{MSD}(\Delta t) = \langle |\delta\mathbf{r}_p(t_0 + \Delta t) - \delta\mathbf{r}_p(t_0)|^2 \rangle_{p, t_0}$$

is averaged over particles and initial times t_0 , with $\delta\mathbf{r}_p = \mathbf{r}_p - \mathbf{r}_{\text{com}}$ the particle position shifted from the center of mass \mathbf{r}_{com} of the system.

where $\langle X_p \rangle_p = 1/N_{\text{tot}} \sum_p X_p$ and $\langle X_\alpha \rangle_\alpha = 1/N \sum_\alpha X_\alpha$ for any quantity X .

E. Spectral decomposition of velocity

1. Periodic boundary conditions

To analyse the spatial modes of the velocity field, we perform a Fourier projection over the mean velocities $\{\bar{\mathbf{v}}_p\}$ at positions $\{\mathbf{r}_p\}$, for the N_{tot} particles. This is preferred to a discrete Fourier transform on a regular grid, where one would need to compute a coarse-grained velocity field for all acquired times, adding more expensive computations. With a Fourier projection, one can directly use the off-grid information on particles positions.

Each Fourier mode for the velocity component in direction i is defined by a wave-vector $\mathbf{k} = (k_x, k_y)$, and one obtains complex coefficients

$$C_i(\mathbf{k}) = \frac{1}{N_{\text{tot}}} \sum_p \bar{v}_{p,i} \exp[-i \mathbf{r}_p \cdot \mathbf{k}] \quad (\text{S15})$$

Because particle velocities are real, one has the spectral redundancy $C_i(-\mathbf{k}) = C_i^*(\mathbf{k})$. Note that the zero mode $C_i(\mathbf{0})$ corresponds to the center-of-mass velocity. For periodic boundary conditions, the wave-vectors \mathbf{k} form a discrete set of modes along each spatial dimension i , $k_i = 2\pi/L_i \mathbb{Z}$ where \mathbb{Z} is the ensemble of signed integers.

To account for temporal director switches, we also project the velocities along $\hat{\mathbf{k}} = \mathbf{k}/|\mathbf{k}|$ and $\hat{\mathbf{k}}_{\perp} = (-k_y, k_x)/|\mathbf{k}|$, such that the Fourier coefficients are

$$C_{\parallel}(\mathbf{k}) = \frac{1}{N_{\text{tot}}} \sum_p (\bar{\mathbf{v}}_p \cdot \hat{\mathbf{k}}) \exp[-i \mathbf{r}_p \cdot \mathbf{k}], \quad (\text{S16})$$

$$C_{\perp}(\mathbf{k}) = \frac{1}{N_{\text{tot}}} \sum_p (\bar{\mathbf{v}}_p \cdot \hat{\mathbf{k}}_{\perp}) \exp[-i \mathbf{r}_p \cdot \mathbf{k}] \quad (\text{S17})$$

An inverse Fourier projection can be defined on a regular grid of spatial points $\{\mathbf{r}\}$ such that

$$\bar{v}_i(\mathbf{r}) = \sum_{\mathbf{k}} C_i(\mathbf{k}) \exp[i \mathbf{r} \cdot \mathbf{k}] \quad (\text{S18})$$

Note that contrarily to a discrete Fourier transform, the projection on the irregular grid of particle's positions $\{\mathbf{r}_p\}$ implies a loss of information when reconstructing the velocities, hence $\bar{\mathbf{v}}(\mathbf{r})$ can be seen as a parameter-free coarse-grained velocity field with weight function $W(\mathbf{R}) = 1/\Omega \sum_{\mathbf{k}} \cos[\mathbf{R} \cdot \mathbf{k}]$ for a system size $\Omega = \prod_{i=1}^d L_i$.

2. Channel geometry

In the channel geometry, due to the confining boundaries, we decompose velocities on an hybrid basis. It is made of Legendre polynomials $P_n(Y)$ in the transverse direction, where $Y = [-1; 1]$, and trigonometric functions $\exp[-i x k_x]$ in the longitudinal direction. The complex coefficients are

$$C_i(k_x, n_y) = \frac{2n_y + 1}{N_{\text{tot}}} \sum_p \bar{v}_{p,i} P_{n_y}(2y_p/W) \exp[-i x_p k_x] \quad (\text{S19})$$

with $n_y \sim \mathbb{N}$ is a positive integer and $k_x = 2\pi/L_x \mathbb{Z}$ as before. An inverse projection can be defined on a regular grid of spatial points $\{\mathbf{r}\}$ such that

$$\bar{v}_i(\mathbf{r}) = \sum_{k_x, n_y} C_i(k_x, n_y) P_{n_y}(2y/W) \exp[i x k_x] \quad (\text{S20})$$

For a simple shear flow $v_x = 2v_0 y/W$ with $k_x = 0$ and $y = [-W/2; W/2]$, one finds coefficients

$$\begin{aligned} C_x(n_y) &= \frac{2n_y + 1}{N_{\text{tot}}} \sum_p v_{p,x} P_{n_y}(2y_p/W) \quad (\text{S21}) \\ &\simeq v_0(n_y + 1/2) \int_{-1}^1 dY Y P_{n_y}(Y) \\ &= v_0 \frac{(2n_y + 1) \sin(\pi n_y)}{\pi(2 - n_y - n_y^2)} \end{aligned}$$

One thus finds $C_x(1) = v_0$ and $C_x(n_y) = 0$ for $n_y \neq 1$. A Legendre decomposition is favored here because the Fourier projection of a simple shear flow $v_x = v_0 \sin(\pi y/W)$ does not select the pure mode $\mathbf{k} = (0, \pi/W)$ as additional modes are non-zero, i.e. the Fourier basis is only complete for periodic functions. For instance, one finds $C_x(k_y) = 2i v_0 z \cos(z\pi/2)/[\pi(1 - z^2)]$ for $k_y = (\pi/W)z$.